Neuron

Article

A bone-derived hormone permits rapid visual escape via GPR37 receptor in a subpopulation of VTA GABAergic neurons

Graphical abstract

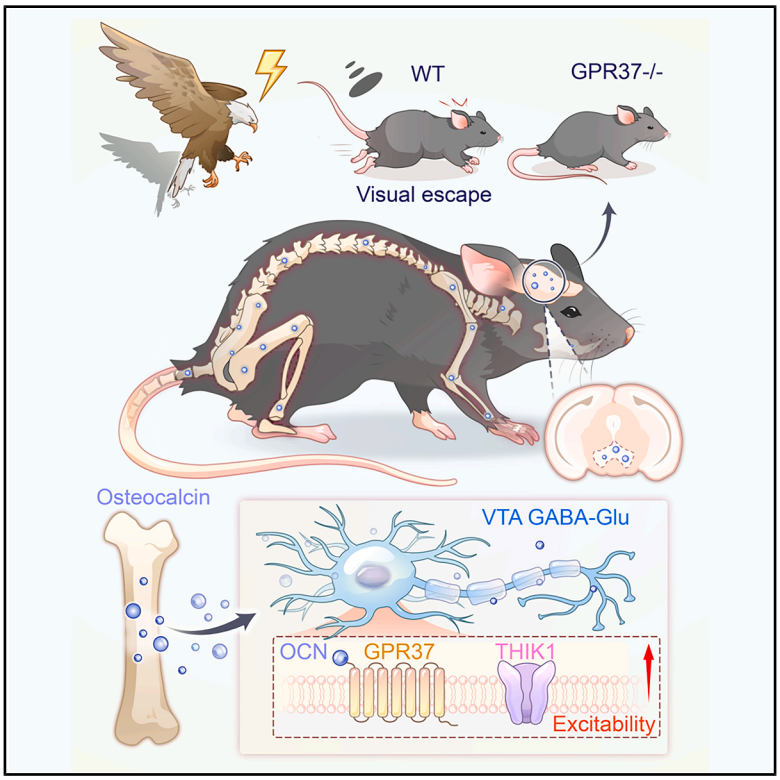

Highlights

- Osteocalcin permits rapid visual escape
- GPR37 in VTA GABA-Glu affects escape
- Osteocalcin enhances VTA GABA-Glu excitability via a non-canonical pathway
- The bone-brain axis is crucial for survival behavior

Authors

Xuemei Liu (刘雪梅), Shuaiyu Wang (王帅毓), Juan Lai (赖娟), ..., Liming Tan (谭力铭), Xiang Li (李翔), Liping Wang (王立平)

Correspondence

xm.liu@siat.ac.cn (X.L.), lm.tan@siat.ac.cn (L.T.), xiang.li@siat.ac.cn (X.L.), lp.wang@siat.ac.cn (L.W.)

In brief

Liu et al. reveal that osteocalcin (OCN) drives rapid visual escape by activating GPR37 in VTA GABA-Glu neurons, enhancing excitability via the OCN-GPR37-cAMP-THIK-1 pathway. This work links bone-derived signals to neural circuits and survival behaviors.

Liu et al., 2026, Neuron *114*, 1–15
May 6, 2026
https://doi.org/10.1016/j.neuron.2025.12.048

CellPress

Please cite this article in press as: Liu et al., A bone-derived hormone permits rapid visual escape via GPR37 receptor in a subpopulation of VTA GABAergic neurons, Neuron (2025), https://doi.org/10.1016/j.neuron.2025.12.048

Neuron

CellPress

Article

A bone-derived hormone permits rapid visual escape via GPR37 receptor in a subpopulation of VTA GABAergic neurons

Xuemei Liu (刘雪梅),[1,2,3,4,5,8,*] Shuaiyu Wang (王帅毓),[1,8] Juan Lai (赖娟),[1,8] Xiang Gao (高翔),[1] Lina Wang (王丽娜),[1,3] Bo Feng (冯博),[1,2,3] Liang Yang (杨靓),[1] Zhengjiang Qian (钱政江),[1,2,3,5] Ruotian Jiang (蒋若天),[7] Jun Chu (储军),[6] Liming Tan (谭力铭),[1,2,3,5,*] Xiang Li (李翔),[1,2,3,5,*] and Liping Wang (王立平)[1,2,3,4,5,9,*]

[1]Shenzhen Key Laboratory of Neuropsychiatric Modulation, Shenzhen-Hong Kong Institute of Brain Science, Shenzhen Institutes of Advanced Technology, Chinese Academy of Sciences, China

[2]Guangdong Provincial Key Laboratory of Brain Connectome and Behavior, Brain Cognition and Brain Disease Institute, Shenzhen Institutes of Advanced Technology, Chinese Academy of Sciences, China

[3]University of Chinese Academy of Sciences, China

[4]Key Laboratory of Brain Cognition and Brain-Inspired Intelligence Technology, Chinese Academy of Sciences, China

[5]Shenzhen University of Advanced Technology, China

[6]CAS Key Laboratory of Health Informatics, Shenzhen Institute of Advanced Technology, Chinese Academy of Sciences, Shenzhen 518055, China

[7]Department of Anesthesiology, West China Hospital, Sichuan University, Chengdu 610041, China

[8]These authors contributed equally

[9]Lead contact

*Correspondence: xm.liu@siat.ac.cn (X.L.), lm.tan@siat.ac.cn (L.T.), xiang.li@siat.ac.cn (X.L.), lp.wang@siat.ac.cn (L.W.)

https://doi.org/10.1016/j.neuron.2025.12.048

SUMMARY

Rapid escape from visual threats is essential for survival, yet the mechanisms establishing its "permissive state" remain poorly understood. Here, we demonstrate that osteocalcin (OCN), a bone-derived hormone, permits rapid visual escape by enhancing the excitability of a ventral tegmental area (VTA) GABAergic neuron subpopulation through the OCN-G Protein-Coupled Receptor 37 (GPR37)-cAMP-TWIK-related halothane-inhibited potassium channel (THIK-1) pathway. Loss of OCN, loss of its receptor GPR37, or conditional deletion of GPR37 in VTA GABAergic or glutamatergic neurons delays escape responses, while reconstituting OCN-GPR37 signaling in the VTA restores normal behavior. Single-cell transcriptomics and electrophysiology reveal that OCN suppresses THIK-1 potassium currents via GPR37-mediated cyclic AMP (cAMP) reduction, thereby increasing neuronal excitability. These findings reveal a novel mechanism through which a bone-derived hormone modulates the excitability of co-releasing neurons to facilitate rapid escape, offering new insights into the regulation of survival behaviors by the bone-brain metabolic axis.

INTRODUCTION

Rapid visual escape is vital for survival, allowing animals to respond swiftly to imminent threats, yet the underlying mechanisms that enable its "permissive state"—a neural and physiological condition priming the brain and body for rapid action—remain poorly understood.[1–6] Looming stimuli, mimicking an approaching predator, are widely used to study visually evoked defensive behaviors, such as freezing, escape, and attack. Extensive research has uncovered distinct neural circuits underlying these responses, involving brain regions responsible for sensory detection, visual-motor transformation, and motor outputs.[7–15] The ventral tegmental area (VTA), traditionally seen as a reward and motivation center,[16–20] has been identified as an information relay for visual escape responses to looming stimuli.[12,21] VTA GABAergic neurons receive visual information from the superior colliculus (SC), and send outputs to the central nucleus of the amygdala (CeA) that elicit visual escape behavior.[12] However, the precise tuning of neuronal excitability and signaling in VTA GABAergic neurons, which creates a heightened readiness to detect, process, and execute immediate motor responses essential for predator evasion, is largely unknown.

Peripherally derived molecules crossing the blood-brain barrier (BBB) are critical for regulating defensive behaviors. Glucocorticoids and adrenaline modulate physiological adaptations, including increased heart rate and respiration, essential for rapid responses.[22–33] Furthermore, osteocalcin (OCN), a protein solely produced in bone and present in the brain and body,[26–29] has recently been identified as a regulator of stress-induced defensive behaviors, including reactions to electrical shock, tail suspension, and 2,4,5-trimethyl thiazoline (TMT) exposure under adrenal insufficiency conditions.[28,30] However, in contrast to the

Please cite this article in press as: Liu et al., A bone-derived hormone permits rapid visual escape via GPR37 receptor in a subpopulation of VTA GABAergic neurons, Neuron (2025), https://doi.org/10.1016/j.neuron.2025.12.048

well-characterized systemic actions of classical stress hormones, the molecular and cellular mechanisms through which OCN modulates neuronal activity to establish a permissive state for stress-induced defensive behaviors remain poorly defined.

This study reveals OCN, a bone-derived hormone, as a key regulator of rapid visual escape, acting through GPR37 in a distinct VTA GABAergic neuron subpopulation. The OCN-GPR37 pathway enhances neuronal excitability by suppressing THIK-1 channels via non-canonical G Protein-Coupled Receptor (GPCR) signaling, redefining the role of skeletal signals in neural circuit modulation. These findings uncover a novel interaction, in which the skeletal system modulates midbrain neuronal properties to orchestrate survival behaviors. By bridging metabolism, neuroscience, and physiology, this work highlights brain-body collaboration in adaptive responses and opens new avenues for exploring metabolic interventions in disorders such as osteoporosis-linked depression and neurodegenerative diseases.

RESULTS

OCN and the GPR37 receptor are required for a rapid visual escape response

OCN, a bone-derived hormone, crosses the BBB and is essential for acute stress responses.[30] To explore its potential involvement in visual defensive behaviors, we first compared circulating levels of undercarboxylated OCN (Gla-OCN) and looming-evoked defensive responses between 3-month-old (young) and 14-month-old (old) wild-type (WT) mice (Figures 1A and 1B). Serum OCN levels were much lower in old mice compared with young mice (Figure 1C, unpaired *t* test). This reduction in OCN correlated with impaired defensive behavior. When exposed to a looming stimulus, old mice exhibited significantly delayed response latency and prolonged return times compared with young mice (Figure 1D, unpaired *t* test). Importantly, this age-related deficit in rapid visual escape was reversible. Intraperitoneal OCN injection restored rapid visual escape in old mice (Figure 1E, paired *t* test). We also investigated whether the looming stimulus itself affects OCN levels. Indeed, exposure to the looming stimulus alone was sufficient to induce an acute rise in circulating OCN levels, and this elevation lasted for at least 30 min, suggesting that OCN acts as a critical mediator of looming-induced defensive behavior (Figure 1F, unpaired *t* test).

To validate that OCN specifically regulates visual defensive responses rather than spontaneous behavioral or anxiety-related changes, we took advantage of OCN knockout (KO) mice, and monitored their spontaneous behavior using a 3D hierarchical behavioral analysis platform (Figure S1A). WT and OCN KO mice exhibited no differences in time spent in the center or in movement speed (Figures S1B and S1C, unpaired *t* test). They also showed no changes in components of spontaneous behaviors, including sniffing, grooming, hunching, jumping, pausing, rearing, running, trotting, and walking (Figure S1D, unpaired *t* test). When assessed in the looming test, $OCN^{-/-}$ mice reproduced the impaired defensive phenotype, similar to the 14-month-old WT mice, exhibiting delayed response latency, longer return times to the nest, and longer duration in the nest (Figure 1G, unpaired *t* test).

To identify the role of two reported OCN-activated receptors, GPR37 and GPR158,[28,34] in visual escape responses, we then tested $GPR37^{-/-}$ and $GPR158^{-/-}$ mice upon looming stimulus. Only $GPR37^{-/-}$ mice exhibited delayed responses and longer return times, while $GPR158^{-/-}$ mice showed no differences (Figure 1G, unpaired *t* test). These results demonstrate that OCN mediates defensive responses primarily through GPR37.

GPR37 in VTA GABAergic and glutamatergic neurons regulates rapid visual escape

The VTA, a hub for looming-evoked defensive responses, is a key target of OCN.[12,29] To test whether local OCN signaling in the VTA could rescue defensive behavior deficits in OCN KO mice, we surgically implanted a cannula connected to a microinjection pump into the VTA of the mice (Figures S2A–S2C). We first confirmed that OCN was nearly undetectable in the serum of OCN KO mice (Figure 2A, unpaired *t* test). Then, local OCN administration in the VTA of OCN KO mice reduced response latency and return time while increasing nest time (Figures 2B and 2C, unpaired *t* test). Similarly, restoring GPR37 in the VTA of $GPR37^{-/-}$ mice via Lenti-GPR37-GFP restored rapid escape responses (Figures 2D–2F and S2D, unpaired *t* test). However, when OCN was administered locally into the VTA of $GPR37^{-/-}$ mice, this treatment failed to rescue the impaired defensive behaviors (Figures 2G and 2H, unpaired *t* test). These results highlight the essential role of the interaction between OCN and GPR37 in the VTA for looming-induced escape behavior. To further confirm that OCN physically binds to GPR37 in VTA neurons, we demonstrated that OCN binds to GPR37 receptors in VTA neurons using biotinylated OCN. Immunostaining revealed streptavidin 488 colocalization with GPR37 in both tyrosine hydroxylase (TH)-positive dopaminergic (DA) neurons and GAD67-positive GABAergic neurons (Figures S3A and S3B). This direct binding evidence strengthens the functional link between OCN and GPR37 in the VTA.

To determine the VTA neuron type mediating OCN-GPR37 signaling in visual escape, we selectively ablated GPR37 in DA, glutamatergic, and GABAergic neurons. Neither global nor VTA-specific GPR37 ablation in DA neurons affected looming responses (Figures 3A–3D and S4, unpaired *t* test). To selectively ablate the GPR37 receptor in VTA glutamatergic or GABAergic neurons, we first tested the specificity and efficiency of our labeling method,[35] followed by validation of the specificity and efficiency of adeno-associated virus (AAV) labeling in VGluT2-ires-Cre and GAD2-ires-Cre mice, with over 90% labeling accuracy and minimal overlap with TH^+ cells (Figures S5A–S5F). Using AAV-CaMKIIα-Cre-GFP or AAV-Dlx5/6-Cre-GFP in $GPR37^{flox/flox}$ mice, we found that selective GPR37 ablation in VTA glutamatergic (Figures 3E and 3F, unpaired *t* test) or GABAergic neurons (Figures 3G and 3H, unpaired *t* test) impaired looming-induced escape responses. These results demonstrate that OCN acts through GPR37 in both glutamatergic and GABAergic neurons within the VTA to mediate looming-induced escape responses.

OCN drives VTA GABAergic neurons into two excitability subpopulations via GPR37/GPR158

VTA GABAergic neurons have been shown to play a critical role in mediating visually evoked innate defensive responses.[12,36] To

Please cite this article in press as: Liu et al., A bone-derived hormone permits rapid visual escape via GPR37 receptor in a subpopulation of VTA GABAergic neurons, Neuron (2025), https://doi.org/10.1016/j.neuron.2025.12.048

CellPress

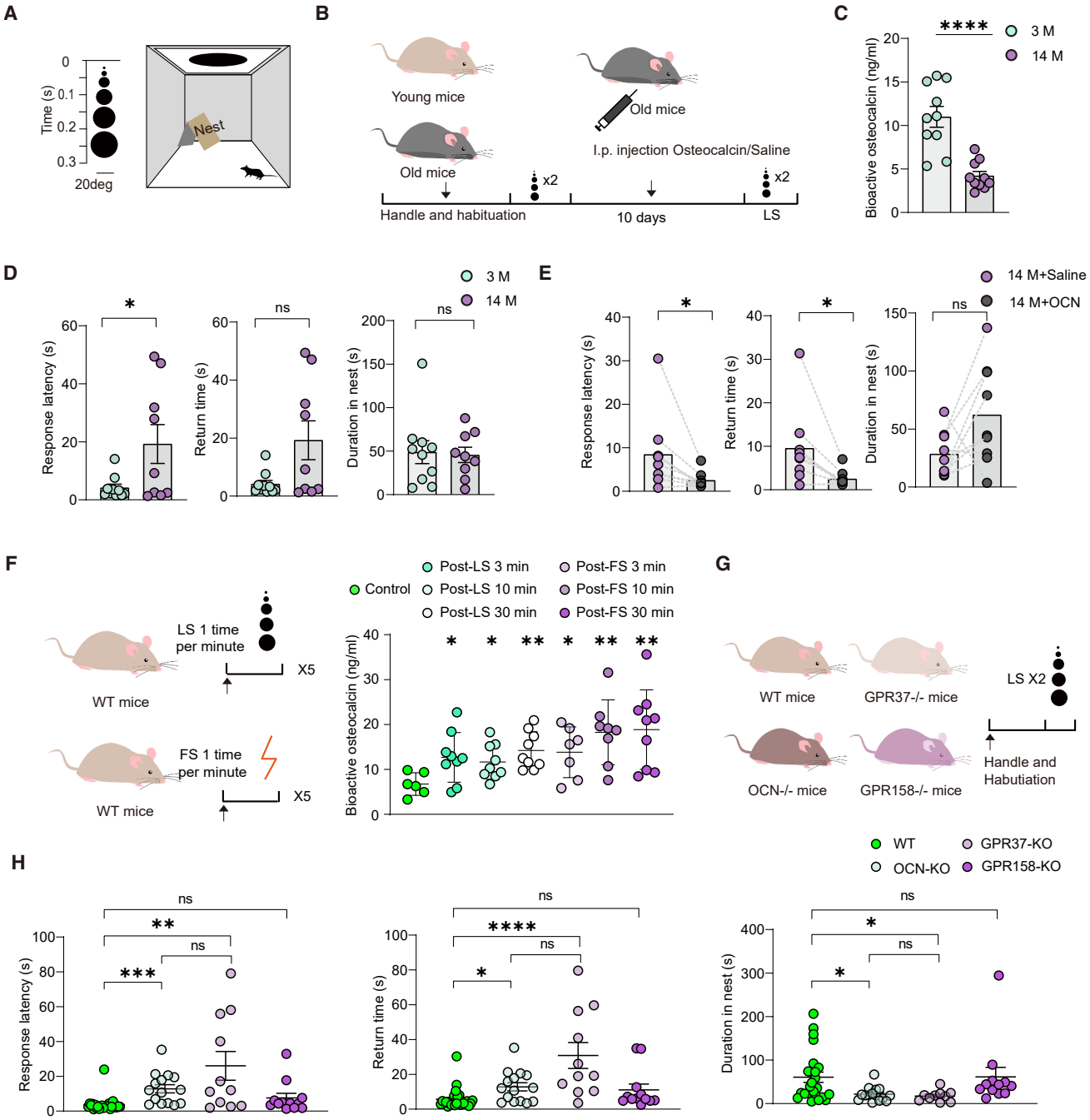

Figure 1. OCN and its receptors mediate innate defensive responses to LS

(A and B) Schematic of behavior paradigm and experimental design.

(C) Serum OCN levels in young (3 months, $n = 10$) and old (14 months, $n = 10$) WT mice.

(D) Bar graphs showing metrics of looming responses of young (3-month-old WT mice, $n = 10$) and old (14-month-old WT mice, $n = 9$) mice.

(E) As in (D), but for old mice (14 months old) after intraperitoneal (i.p.) injection (saline group, $n = 9$; OCN group, $n = 9$).

(F and G) Serum OCN measurement following footshock (FS) and repetitive looming stimulus (LS) ($n = 6$ for control, $n = 7$ for post FS 3 min, $n = 8$ for post FS 10 min, and $n = 9$ for post FS 30 min; $n = 6$ for control, $n = 9$ for post LS 3, 10, and 30 min).

(H) Bar graphs showing metrics of looming responses of WT ($n = 25$), OCN KO mice ($n = 15$), GPR37 KO ($n = 11$), and GPR158 KO mice ($n = 12$).

Data are shown as mean ± SEM. Unpaired Student's t test for (C), (D), (F), and (H) and paired Student's t test for (E). $^{*}p < 0.05$, $^{**}p < 0.01$, $^{***}p < 0.001$, $^{****}p < 0.0001$; ns, not significant.

Please cite this article in press as: Liu et al., A bone-derived hormone permits rapid visual escape via GPR37 receptor in a subpopulation of VTA GABAergic neurons, Neuron (2025), https://doi.org/10.1016/j.neuron.2025.12.048

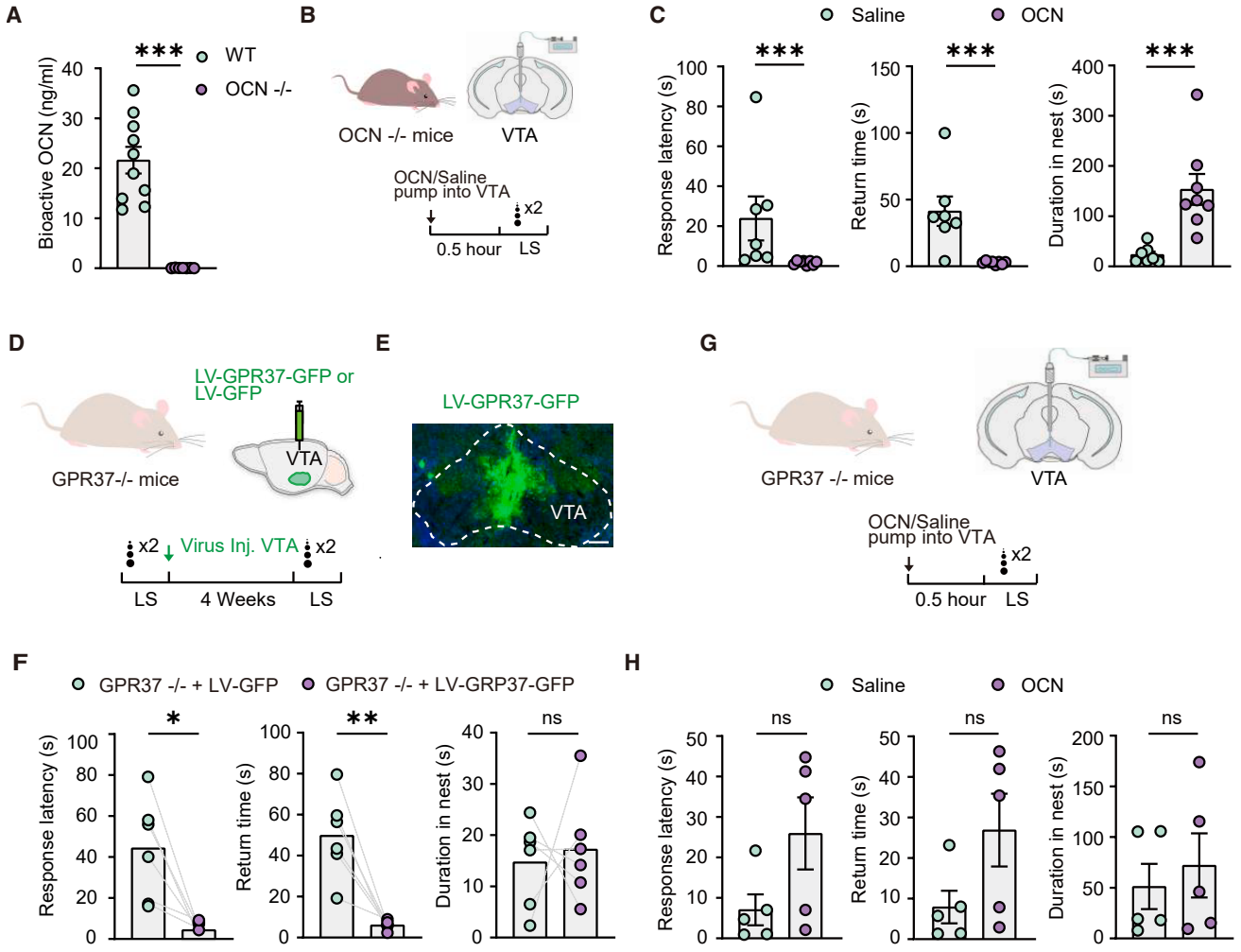

Figure 2. Intact OCN-GPR37 signaling in the VTA is required for rapid visual escape

(A) Plasma bioactive OCN levels in WT (n = 10) and OCN KO mice (n = 7).
(B) Schematic of the experimental procedure for intra-VTA infusion of OCN or saline, followed by LS.
(C) Behavioral analysis in OCN KO mice after intra-VTA OCN administration (saline, n = 7; OCN, n = 8).
(D) Experimental timeline for re-expression of GPR37 in GPR37$^{-/-}$ mice
(E) Fluorescent image showing LV-GPR37-GFP expression in the VTA. Scale bar, 200 μm.
(F) Behavioral changes in GPR37$^{-/-}$ mice after VTA-targeted GPR37 restoration (LV-GFP, n = 6; LV-GPR37-GFP, n = 6).
(G) Schematic of intra-VTA OCN/saline infusion in GPR37$^{-/-}$ mice, followed by LS.
(H) Behavioral analysis in GPR37 mice after intra-VTA OCN administration (saline, n = 5; OCN, n = 5).
Data are shown as mean ± SEM. Unpaired Student's t test for (A), (C), (F), and (H). *p < 0.05, **p < 0.01, ***p < 0.001; ns, not significant.

investigate how OCN affected VTA GABAergic neurons, we performed whole-cell patch-clamp recordings in GAD2-ires-Cre mice with AAV-DIO-GFP injection in the VTA (Figure 4A). By using unimodal-bimodal testing, 24 recorded VTA GABAergic neurons were classified into one group (Figure 4B, Hartigan's dip test, p = 0.7814). After 15 min of OCN (10 ng/mL) infusion, they were classified into two distinct subpopulations (type I neurons and type II neurons; Hartigan's dip test, p = 0.073). To further validate the OCN-induced bipartite classification, we performed K-means clustering analysis on the same dataset of neuronal excitability changes. This analysis yielded an average silhouette coefficient of 0.865, which indicates that neurons within each cluster were highly similar to one another, whereas neurons between the two clusters were distinctly different, supporting that OCN specifically drives the differentiation of VTA GABAergic neurons into two functionally distinct subpopulations.

A key question arising from this finding was whether these OCN-induced divisions of VTA GABAergic neurons were due to pre-existing variability in the neurons' intrinsic properties. To address this, we first analyzed the basal electrophysiological characteristics of the two subpopulations (type I neurons and type II neurons) prior to OCN treatment. Notably, under basal conditions, type I neurons exhibited a significantly lower spontaneous action potential rate compared with type II

Please cite this article in press as: Liu et al., A bone-derived hormone permits rapid visual escape via GPR37 receptor in a subpopulation of VTA GABAergic neurons, Neuron (2025), https://doi.org/10.1016/j.neuron.2025.12.048

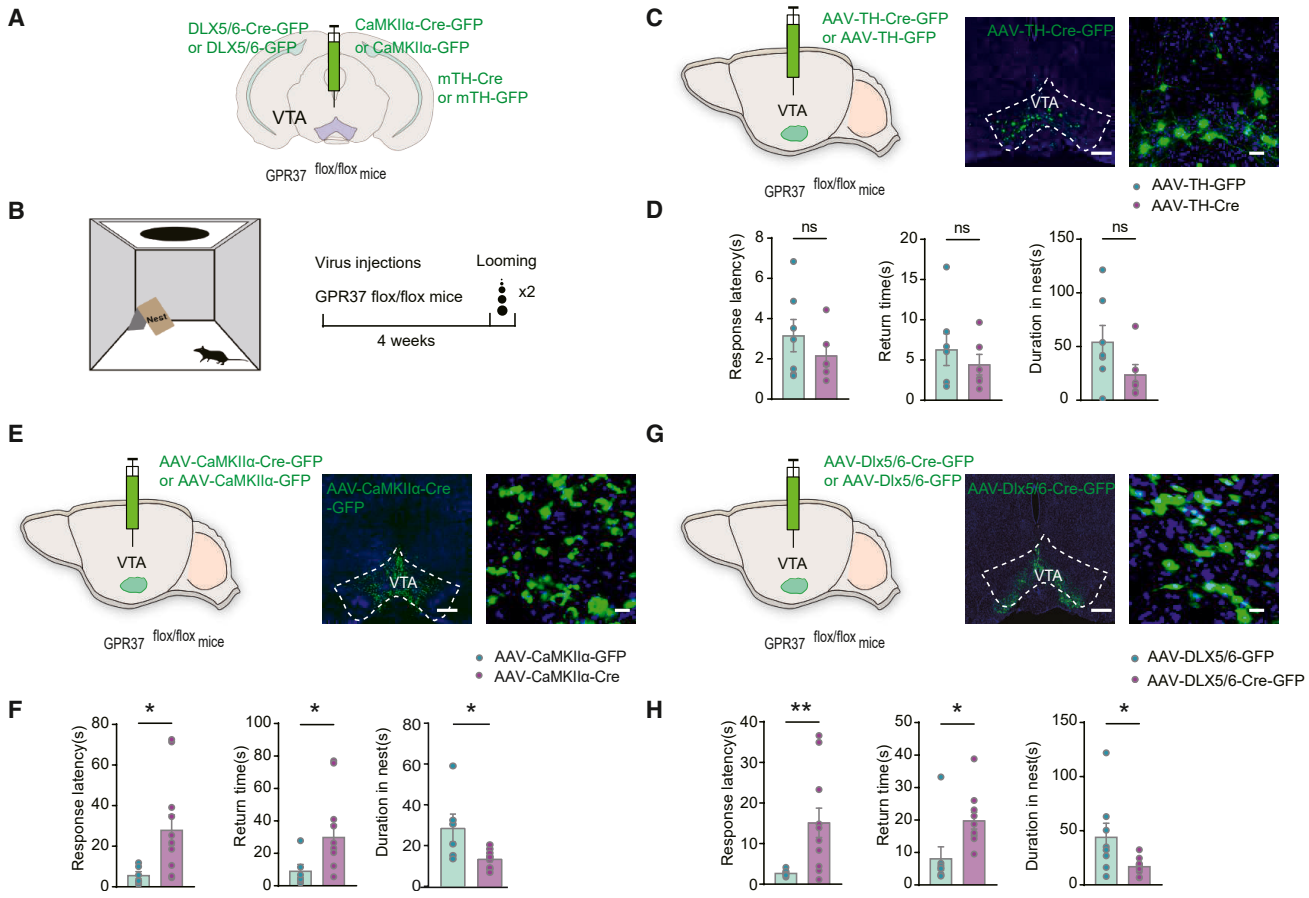

Figure 3. Cell-type-specific manipulation of GPR37 in VTA and its effects on visual defensive behaviors

(A) Schematic of deletion of GPR37 from VTA-specific neuron populations.

(B) Schematic of looming test and experimental timeline.

(C) Schematic of AAV-TH-Cre-GFP or AAV-TH-GFP injection into the VTA of GPR37$^{flox/flox}$ mice, with fluorescent images of virus expression in VTA. Scale bar, 200 μm (left) and 10 μm (right).

(D) Behavioral analysis in GPR37$^{flox/flox}$ mice after AAV-TH-Cre (n = 7) or AAV-TH-GFP (n = 6) injection.

(E) Schematic of AAV-CaMKIIα-Cre-GFP or AAV-CaMKIIα-GFP injection into the VTA of GPR37$^{flox/flox}$ mice, with fluorescent images of virus expression in VTA. Scale bar, 200 μm (left) and 10 μm (right).

(F) Behavioral analysis in GPR37$^{flox/flox}$ mice after AAV-CaMKIIα-Cre-GFP (n = 6) or AAV-CaMKIIα-GFP (n = 10) injection.

(G) Schematic of AAV-Dlx5/6-Cre-GFP or AAV-Dlx5/6-GFP injection into the VTA of GPR37$^{flox/flox}$ mice, with fluorescent images of virus expression in VTA. Scale bar, 200 μm (left) and 10 μm (right).

(H) Behavioral analysis in GPR37$^{flox/flox}$ mice after AAV-Dlx5/6-Cre-GFP (n = 8) or AAV-Dlx5/6-GFP (n = 10) injection.

Data are shown as mean ± SEM. Unpaired Student's t test for (D), (F), and (H). *$p < 0.05$, **$p < 0.01$; ns, not significant.

neurons (Figure 4C, unpaired t test). In contrast, other membrane properties showed no significant differences between the two subpopulations (Figure S6, unpaired t test). We then investigated how OCN modulated the excitability of these two inherently distinct subpopulations. Following 15 min of OCN (10 ng/mL) infusion, type I neurons, which displayed a relatively lower basal excitability, showed a significant increase in spontaneous action potential rate (Figure 4D, paired t test). In contrast, type II neurons, characterized by higher basal excitability, exhibited a notable reduction in spontaneous action potential rate after OCN treatment (Figure 4E, paired t test).

To explore whether these changes in neuronal excitability were caused by changes in synaptic activity, we recorded spontaneous excitatory postsynaptic currents (sEPSCs) and spontaneous inhibitory postsynaptic currents (sIPSCs) in VTA GABAergic neurons. We observed no significant changes in the amplitude or frequency of sEPSCs and sIPSCs following OCN treatment (Figures S7A–S7F, paired t test), indicating that the OCN-induced alterations in spontaneous action potential rates were not driven by changes in synaptic transmission.

To further identify the molecular basis of these two subpopulations, we explored whether they correspond to the two known OCN-activated receptors, GPR37 and GPR158, by performing whole-cell patch-clamp recordings in GPR37$^{-/-}$ and GPR158$^{-/-}$ mice injected with AAV-Dlx5/6-GFP, respectively

Please cite this article in press as: Liu et al., A bone-derived hormone permits rapid visual escape via GPR37 receptor in a subpopulation of VTA GABAergic neurons, Neuron (2025), https://doi.org/10.1016/j.neuron.2025.12.048

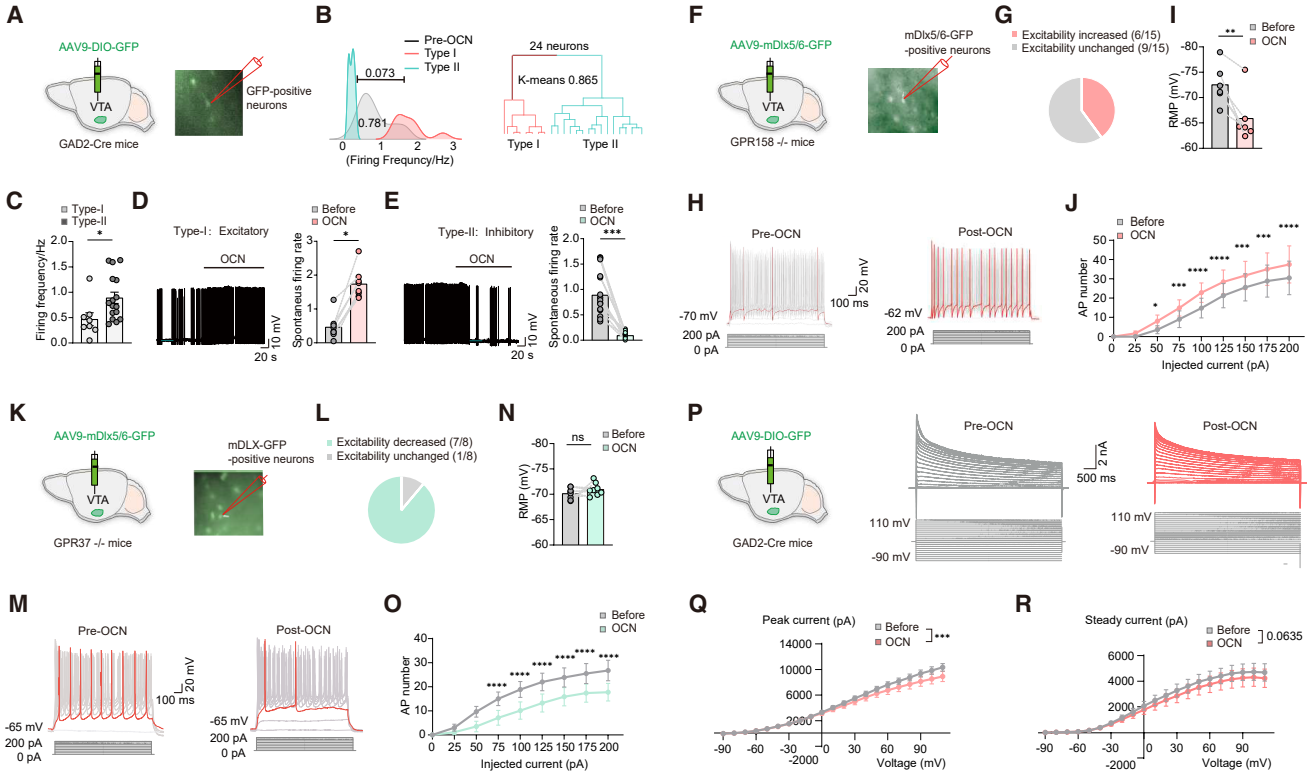

Figure 4. OCN elicits excitatory or inhibitory responses in distinct subpopulations of VTA GABAergic neurons

(A) Schematic of AAV9-DIO-GFP injection into the VTA of GAD2-Cre mice, with fluorescent image of GFP-positive neurons.
(B) Left: firing frequency distribution of VTA neurons pre OCN (cyan) and classified into type I (red) and type II (pink). Right: K-means clustering of 24 neurons into type I and type II.
(C) Firing frequency of type I (n = 8) and type II (n = 16) neurons.
(D) Representative traces (left) and quantification (right) of spontaneous firing rate in type I neurons pre and post OCN (n = 8).
(E) Representative traces (left) and quantification (right) of spontaneous firing rate in type II neurons pre and post OCN (n = 16).
(F) Schematic of AAV9-mDlx5/6-GFP injection into the VTA of GPR158$^{-/-}$ mice, with fluorescent image of mDlx5/6-GFP-positive neurons.
(G) Pie chart showing proportion of neurons with increased (red) or unchanged (gray) excitability post OCN.
(H) Representative traces of neuronal firing pre and post OCN.
(I) Resting membrane potential (RMP) of neurons pre and post OCN (n = 6).
(J) Comparisons of the number of action potentials evoked by injected positive currents before and after OCN application (n = 6).
(K) Schematic of AAV9-mDlx5/6-GFP injection into the VTA of GPR37$^{-/-}$ mice, with fluorescent image of mDlx-GFP-positive neurons.
(L) Pie chart showing proportion of neurons with decreased (cyan) or unchanged (gray) excitability post OCN.
(M) Representative traces of neuronal firing pre and post OCN.
(N) RMP of neurons pre and post OCN (n = 8).
(O) Comparisons of the number of action potentials evoked by injected positive currents before and after OCN application (n = 8).
(P) Schematic of AAV9-DIO-GFP injection into the VTA of GAD2-Cre mice, with representative traces of voltage-clamp recordings pre and post OCN.
(Q) Comparisons of peak and steady-state potassium currents before and after OCN application (n = 10).
Data are shown as mean ± SEM. Hartigan's dip test for (B); unpaired Student's t test for (C); paired Student's t test for (D), (E), and (I); and two-way ANOVA for (J), (O), (Q), and (R) . *p < 0.05, **p < 0.01, ***p < 0.001, ****p < 0.0001; ns, not significant.

(Figures 4F and 4K). In GPR158$^{-/-}$ mice, we could not detect the type II (inhibition-prone) neuron population following OCN infusion (Figure 4G). OCN decreased the resting membrane potential (Figures 4H and 4I, paired t test) and increased the neuronal excitability (Figure 4J, two-way ANOVA with Sidak test for post hoc corrections). Conversely, in GPR37$^{-/-}$ mice, the type I (excitation-prone) neuron population was undetectable after OCN treatment (Figure 4L). OCN treatment did not affect the resting membrane potential (Figures 4M and 4N) but decreased the neuronal action potential firing (Figure 4O, two-way ANOVA with Sidak test for post hoc corrections).

OCN has been shown to regulate neuronal excitability by modulating potassium currents.[37] To investigate whether OCN modulates gross potassium currents in VTA GABAergic neurons, we performed recordings in GAD2-ires-Cre mice with AAV-DIO-GFP (Figure 4P) and found that OCN infusion reduced both peak and steady-state potassium currents compared with the baseline (Figures 4Q and 4R, two-way ANOVA). These results demonstrate that OCN drives VTA GABAergic neurons into two

Please cite this article in press as: Liu et al., A bone-derived hormone permits rapid visual escape via GPR37 receptor in a subpopulation of VTA GABAergic neurons, Neuron (2025), https://doi.org/10.1016/j.neuron.2025.12.048

CellPress

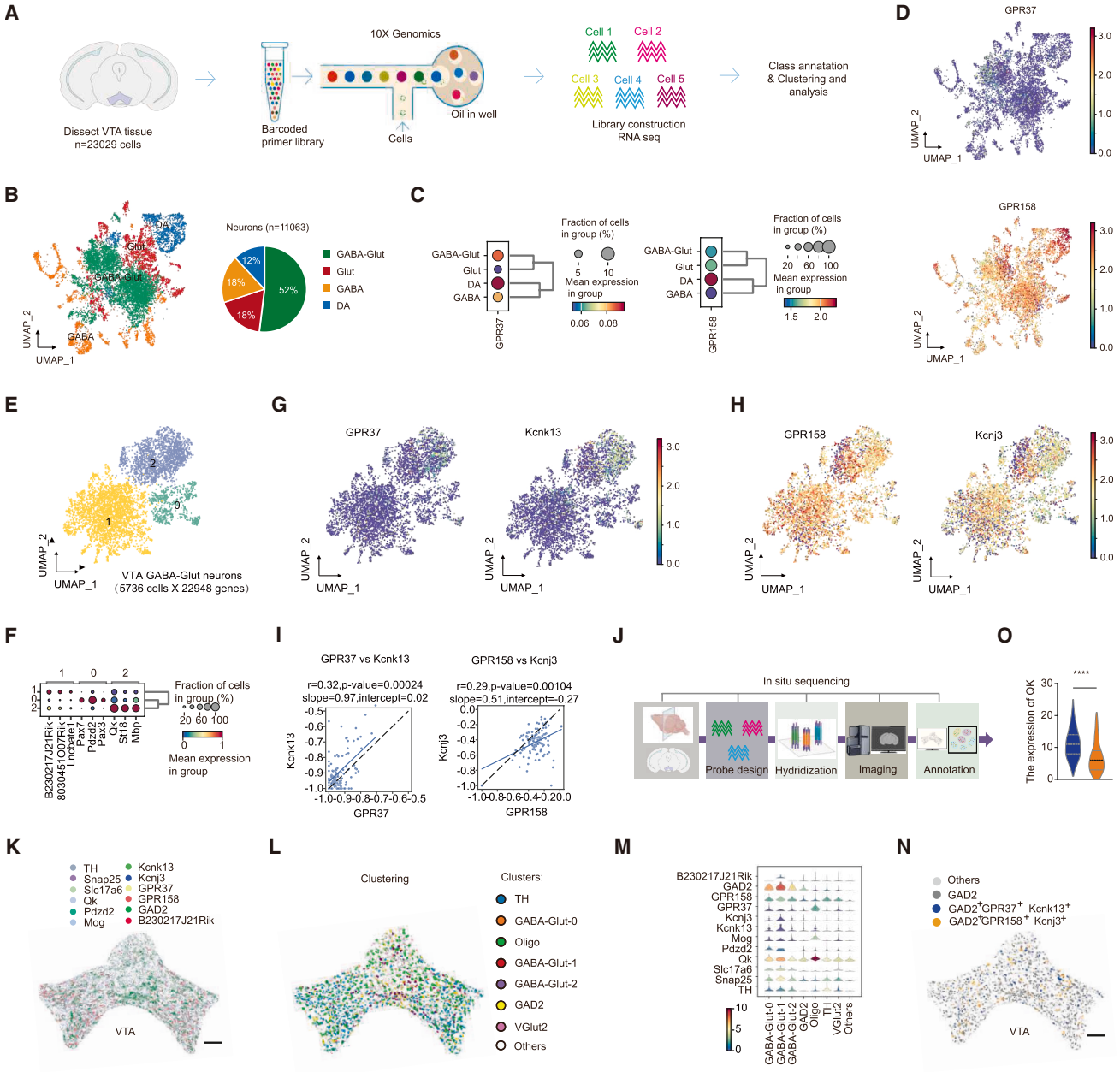

Figure 5. snRNA-seq characterized GPR37, GPR158 receptors, and their co-expressed potassium channels in distinct neuronal populations in the VTA

(A) VTA snRNA-seq workflow.
(B) UMAP plot of the proportion of neuronal populations within the VTA.
(C) Dot plots showing the expression levels of GPR37 and GPR158 in different neuronal populations within VTA.
(D) GPR37 and GPR158 expression shown in the UMAP.
(E) Clustering of VTA GABA-Glut neurons identified 3 subtypes.
(F) Marker gene expression of 3 subtypes in (A).
(G) Expression of GPR37 and Kcnk13 in 3 subtypes in UMAP plot.
(H) Expression of GPR158 and Kcnj3 in 3 subtypes in UMAP plot.
(I) Pearson correlation of GPR37 and Kcnk13 expression, with *p* value, slope and intercept of linear regression.
(J) Workflow of the *in situ* sequencing.
(K) Spatial transcriptomics images in the VTA. Scale bar, 200 μm.
(L) Heatmap of marker gene expression in cell clusters.
(M) Violin plot of marker gene expression in each cluster.
(N and O) Spatial transcriptomics expression of GPR37+ Kcnk13+ GAD2+ and GPR158+ Kcnj3+ GAD2+ subclusters.

Please cite this article in press as: Liu et al., A bone-derived hormone permits rapid visual escape via GPR37 receptor in a subpopulation of VTA GABAergic neurons, Neuron (2025), https://doi.org/10.1016/j.neuron.2025.12.048

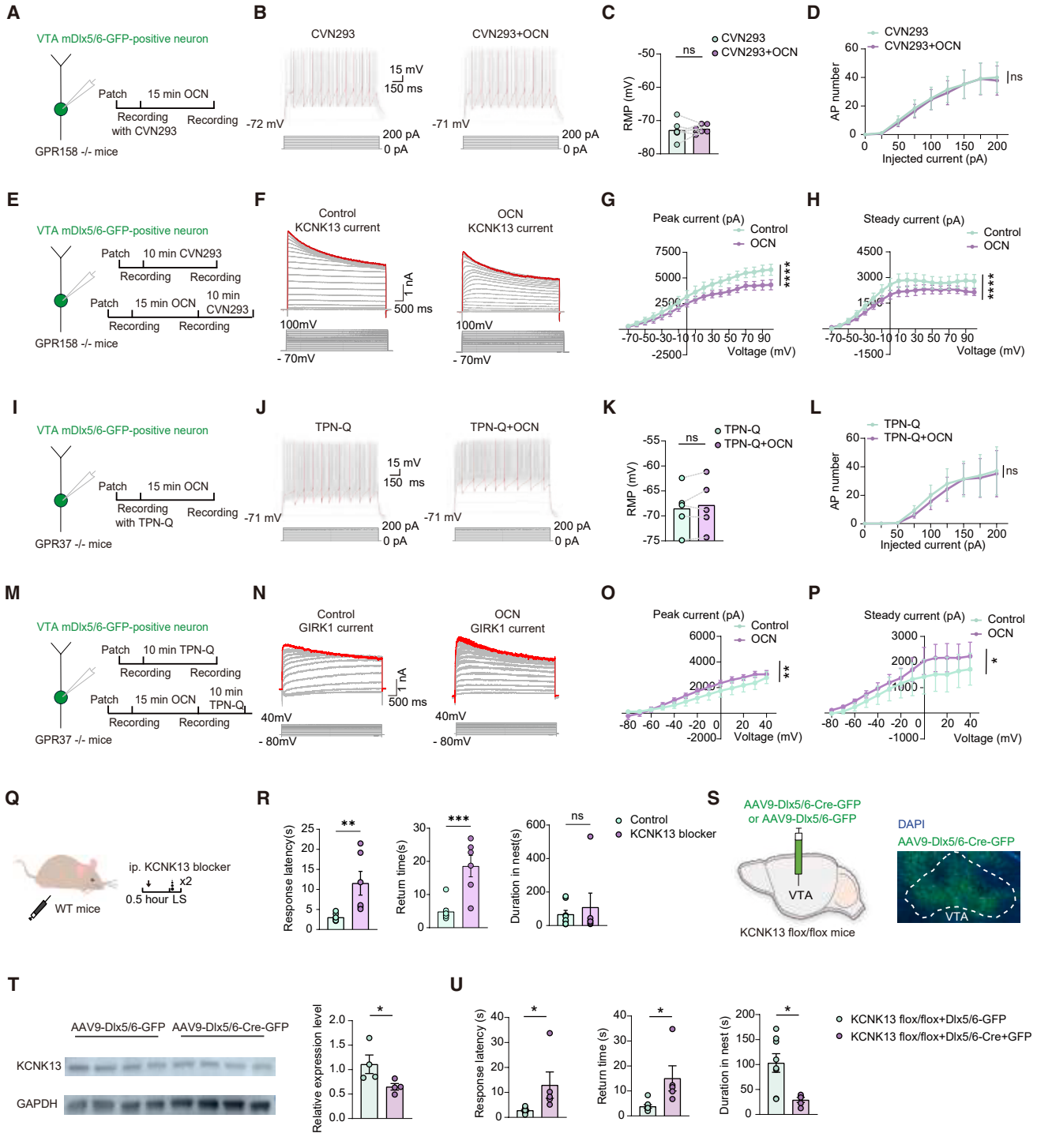

Figure 6. Roles of KCNK13 and GIRK1 channels in OCN-mediated modulation of VTA neuronal excitability and behavior

(A) Schematic of current-clamp recording from VTA mDlx5/6-GFP-positive neurons in GPR158$^{-/-}$ mice, with OCN application and CVN293 treatment.

(B) Representative traces of neuronal firing in CVN293-treated and CVN293 + OCN-treated groups.

(C) Quantification of RMP in CVN293 and CVN293 + OCN groups (n = 6).

(D) Number of action potentials evoked by injected current in CVN293 and CVN293 + OCN groups (n = 6).

(E) Schematic of voltage-clamp recordings from VTA mDlx5/6-GFP-positive neurons in GPR158 mice, with experimental design.

(F) Representative traces of KCNK13 current in control and OCN-treated groups.

(G and H) Peak and steady-state KCNK13 current in control (n = 10) and OCN groups (n = 10).

(legend continued on next page)

excitability subpopulations via GPR37/GPR158 and plays a role in modulating their K^+ currents.

Distinct potassium channels are co-expressed with the two GPRs in VTA

The VTA, a heterogeneous nucleus linked to reward, motivation, alertness, and neuropsychiatric disorders,[20] requires detailed cellular characterization to explore GPR37's role in visual escape. Using the 10× Chromium platform,[38] we performed single-nucleus RNA sequencing (snRNA-seq) on VTA tissues from male mice, yielding 23,029 high-quality nuclear transcriptomes after filtering (Figure 5A). Using uniform manifold approximation and projection (UMAP) and unsupervised clustering, we constructed a VTA cell-type atlas, classifying cells into neurons (n = 11,063) and non-neuronal cells (n = 11,685) based on Snap25 expression (Figures S8A–S8C). Neurons comprised Glut (n = 2,038), GABA (n = 1,966), GABA-Glut (n = 5,736), and DA types (n = 1,323), defined by canonical markers (Figures 5A, 5B, and S8A). GABA-Glut neurons constituted over half of all neurons and 70% of those expressing GABAergic or glutamatergic markers (Figure 5B).

We analyzed GPR37 and GPR158 expression across neuronal types, revealing distinct patterns. GPR158 was broadly expressed at high levels, whereas GPR37 was restricted to DA and GABAergic neurons (pure-GABA and GABA-Glut) at lower levels and absent in Glut-only neurons (Figures 5C, 5D, and S8D). Given the role of GPR37 in VTA GABAergic and glutamatergic, but not DA neurons, in mediating looming escape behavior, we focused on VTA GABAergic neurons, of which 70% co-express glutamatergic markers and exhibit higher GPR37 levels.

To identify potassium channel genes with expression patterns correlated with GPR37 and GPR158 expression in VTA GABAergic neurons, we focused on GABA-Glut neurons to reduce data complexity; unsupervised clustering revealed three subtypes with distinct marker genes (Figures 5E and 5F). GPR37 was expressed in subtype 2 at the highest level, while GPR158 was enriched in subtype 1 (Figures 5G and 5H). Among 71 potassium channel genes expressed in VTA GABA-Glut neurons (Figure S9), Pearson correlation analysis identified Kcnk13 (K2P13.1) and Kcnj3 as the top candidates downstream of GPR37 and GPR158, respectively, based on correlation strength, p value (<0.01), and regression metrics (Figures 5I, S10, and S11; Tables S1 and S2).

To map the spatial organization of neuronal subtypes, we analyzed the expression and distribution of 12 genes (Figures 5J and 5K) and identified 8,133 neurons and 1,079 oligodendrocytes across two replicates. *In situ* sequencing revealed seven transcriptionally and spatially defined clusters, including three GABA-Glut subtypes consistent with snRNA-seq results (Figures 5J–5M). Although subtype 2 marker Qk was enriched in $GPR37^+KCNK13^+GAD2^+$ cells compared with $GPR158^+KCNJ3^+GAD2^+$ cells, these two types of $GAD2^+$ cells did not show clear spatial segregation (Figures 5N and 5O).

OCN increases excitability of VTA GABAergic neuron subpopulations via the GPR37-K2P13.1 axis

To further confirm the receptor-dependent association between OCN, potassium channels, and neuronal excitability, we performed experiments in $GPR158^{-/-}$ and $GPR37^{-/-}$ mice injected with AAV-Dlx5/6-GFP in the VTA. In $GPR158^{-/-}$ mice, pre-application of CVN293, a specific KCNK13 channel inhibitor,[39] alone depolarized the resting membrane potential and increased the VTA GABAergic neuron excitability elicited by a series of positive currents (Figures S12A–S12D, two-way ANOVA with Sidak test for post hoc corrections). The subsequent application of OCN did not induce further changes in either resting membrane potential or neuronal excitability (Figures 6A–6D, paired t test, two-way ANOVA with Sidak test for post hoc corrections). Consistent with this, voltage-clamp recordings revealed that OCN significantly inhibited both KCNK13 peak and steady-state currents in $GPR158^{-/-}$ VTA GABAergic neurons (Figures 6E–6H, two-way ANOVA), confirming that OCN modulates KCNK13 channels to regulate excitability in a GPR37-dependent manner. Conversely, in $GPR37^{-/-}$ mice, pre-application of tertiapin-Q (TPN-Q, a specific KCNJ3 channel inhibitor[40]) alone depolarized the resting membrane potential and elevated neuronal excitability (Figures S12E–S12H, paired t test, two-way ANOVA with Sidak test for post hoc corrections). Subsequent addition of OCN failed to alter this excitability further (Figures 6I–6L, paired t test, two-way ANOVA with Sidak test for post hoc corrections). Voltage-clamp recordings showed that OCN enhanced KCNJ3 currents in $GPR37^{-/-}$ VTA GABAergic neurons (Figures 6M–6P, two-way ANOVA), verifying that OCN acts through GPR 158 to reduce excitability via KCNJ3 channels.

Building on the *in vitro* findings that OCN modulates KCNK13 to regulate GPR37-dependent neuronal excitability in

(I) Schematic of current-clamp recording from VTA mDlx5/6-GFP-positive neurons in $GPR37^{-/-}$ mice, with OCN application and TPN-Q treatment.
(J) Representative traces of neuronal firing in TPN-Q-treated and TPN-Q + OCN-treated groups.
(K) Quantification of RMP in TPN-Q and TPN-Q + OCN groups (n = 6).
(L) Number of action potentials evoked by injected current in TPN-Q and TPN-Q + OCN groups (n = 6).
(M) Schematic of voltage-clamp recording from VTA mDlx5/6-GFP-positive neurons in $GPR37^{-/-}$ mice, with experimental design.
(N) Representative traces of GIRK1 current in control and OCN-treated groups.
(O and P) Peak and steady-state GIRK1 current in control (n = 10) and OCN groups (n = 10).
(Q) Schematic of intraperitoneal (i.p.) injection of KCNK13 blocker in WT mice, followed by LS testing after 0.5 h.
(R) Behavioral analysis after KCNK13 blocker injection (control, n = 8; KCNK13 blocker, n = 6).
(S) Schematic of AAV9-Dlx5/6-Cre-GFP or AAV9-Dlx5/6-GFP injection into the VTA of $KCNK13^{flox/flox}$ mice, with fluorescent image of VTA.
(T) Western blot analysis of KCNK13 protein expression in $KCNK13^{flox/flox}$ mice after virus injection (AAV9-Dlx5/6-GFP, n = 4; AAV9-Dlx5/6-Cre-GFP, n = 4).
(U) Behavioral analysis in $KCNK13^{flox/flox}$ mice after AAV-mediated KCNK13 manipulation (AAV9-Dlx5/6-GFP, n = 8; AAV9-Dlx5/6-Cre-GFP, n = 5).
Data are shown as mean ± SEM. Unpaired Student's t test for (R), (T), and (U); paired Student's t test for (C) and (K); and two-way ANOVA for (D), (G), (H), (L), (O), and (P). $^*p < 0.05$, $^{**}p < 0.01$, $^{***}p < 0.001$, $^{****}p < 0.0001$; ns, not significant.

Please cite this article in press as: Liu et al., A bone-derived hormone permits rapid visual escape via GPR37 receptor in a subpopulation of VTA GABAergic neurons, Neuron (2025), https://doi.org/10.1016/j.neuron.2025.12.048

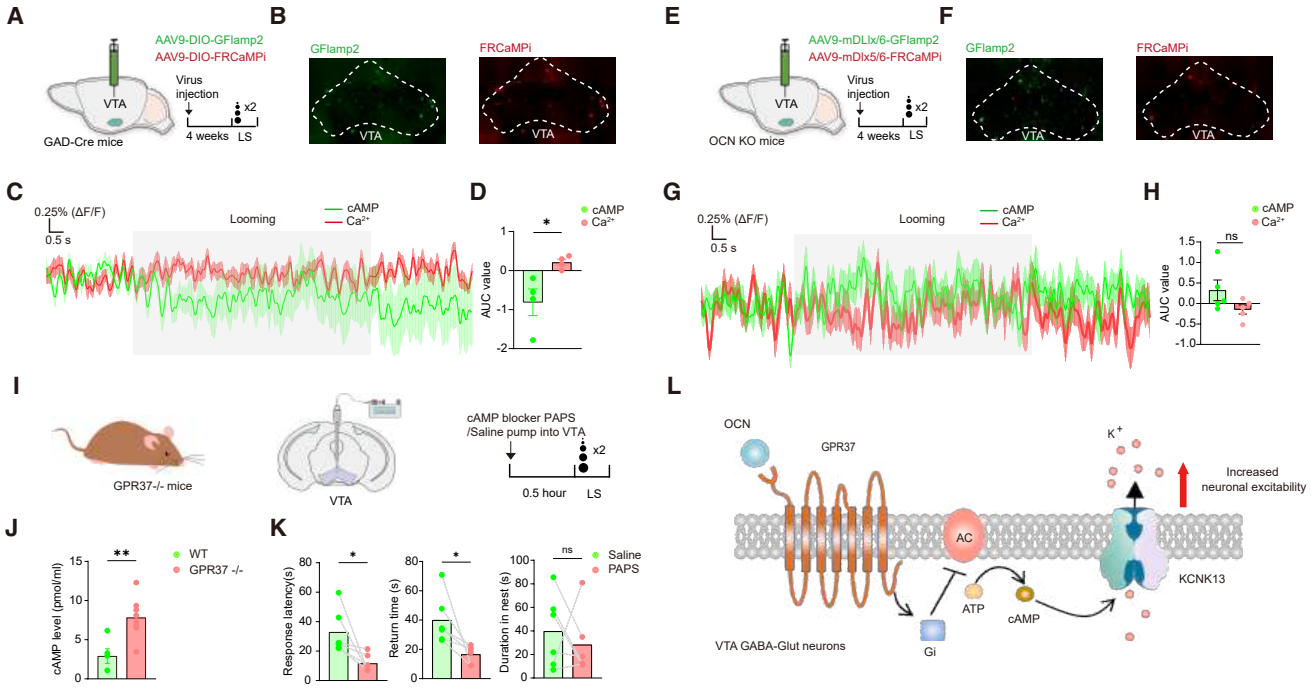

Figure 7. GPR37 is required for the cAMP level reduction in the VTA, which is essential for rapid visual escape

(A) Schematic of AAV9-DIO-GFlamp2 and AAV9-DIO-FRCaMPi injection into the VTA of GAD-Cre mice, with LS tests after 4 weeks.
(B) Fluorescent images of GFlamp2 (green) and FRCaMPi (red) expression in VTA.
(C) Traces of cAMP (green) and Ca^{2+} (red) responses to LS in VTA neurons.
(D) Quantification of area under the curve (AUC) for cAMP ($n = 4$) and Ca^{2+} responses ($n = 4$)
(E) Schematic of AAV9-mDlx5/6-GFlamp2 and AAV9-mDlx5/6-FRCaMPi injection into the VTA of OCN KO mice, with LS tests after 4 weeks.
(F) Fluorescent images of GFlamp2 (green) and FRCaMPi (red) expression in VTA of OCN KO mice.
(G) Traces of cAMP (green) and Ca^{2+} (red) responses to LS in VTA neurons of OCN KO mice.
(H) Quantification of AUC for cAMP ($n = 5$) and Ca^{2+} responses ($n = 5$) in OCN KO mice.
(I) Schematic of intra-VTA infusion of cAMP blocker PAPS or saline in $GPR37^{-/-}$ mice, followed by LS testing after 0.5 h.
(J) cAMP levels in WT ($n = 5$) and $GPR37^{-/-}$ ($n = 8$) mice.
(K) Comparisons of looming-evoked escape between saline ($n = 6$) and PAPS ($n = 6$) groups.
(L) Model of OCN-GPR37 signaling in VTA GABA-Glut neurons.
Data are shown as mean ± SEM. Unpaired Student's *t* test for (D), (H), (J), and (K). $^{*}p < 0.05$, $^{**}p < 0.01$; ns, not significant.

VTA GABAergic subpopulations, we next tested whether this KCNK13-mediated mechanism translates to *in vivo* visual escape behavior. Notably, intraperitoneal injection of the KCNK13 blocker CVN293 (5 mg/kg) impaired rapid visual escape behavior when mice were exposed to looming stimuli, resulting in longer response latency and return time (Figures 6Q and 6R, unpaired *t* test). To further confirm the cell-type-specific role of KCNK13 in rapid visual escape, we used $KCNK13^{flox/flox}$ mice to specifically ablate KCNK13 in VTA GABAergic neurons by injecting AAV-Dlx5/6-Cre-GFP (control group: AAV-Dlx5/6-GFP; Figure 6S). We first confirmed the viral expression in VTA and a reduction in KCNK13 protein levels (Figure 6T, unpaired *t* test). Behavioral tests revealed that these conditional KO mice exhibited a phenotype highly similar to CVN293-treated mice. When exposed to looming stimuli, they failed to initiate rapid escape behavior, with longer response latency, return time, and duration in nest compared with the control group (Figure 6U, unpaired *t* test). This *in vivo* genetic evidence, combined with the pharmacological data, confirms that KCNK13 in VTA GABAergic neurons is a critical downstream mediator of OCN-GPR37 signaling for looming-induced visual escape.

GPR37 reduces cAMP levels in the VTA via the non-canonical Gi pathway to facilitate rapid visual escape

Both single-cell transcriptomics and electrophysiological evidence identified Kcnk13, encoding K2P13.1 (THIK-1) channels, as a downstream target of OCN-GPR37 signaling. Previous studies showed that GPR37 activation leads to a cyclic AMP (cAMP) reduction.[41–45] To examine whether cAMP is involved in looming-induced visual escape, we specifically expressed cAMP probes (GFlamp2) and Ca^{2+} probes (FRCaMPi) in VTA GABAergic neurons by injecting AAV-DIO-GFlamp2 and AAV-DIO-FRCaMPi into the VTA of GAD-Cre mice (Figure 7A). We used fluorescence immunostaining to confirm that the viral vectors were expressed in the VTA (Figure 7B). When these mice were exposed to looming stimuli, a significant decrease in cAMP fluorescence intensity and a concurrent increase in Ca^{2+} fluorescence intensity in VTA GABAergic neurons were observed (Figures 7C and 7D,

Please cite this article in press as: Liu et al., A bone-derived hormone permits rapid visual escape via GPR37 receptor in a subpopulation of VTA GABAergic neurons, Neuron (2025), https://doi.org/10.1016/j.neuron.2025.12.048

unpaired *t* test). To confirm that OCN is the upstream trigger for this cAMP/Ca^{2+} response to the looming stimulus, we next performed the same experiment in OCN KO mice. We injected AAV-Dlx5/6-GFlamp2 and AAV-Dlx5/6-FRCaMPi into the VTA of OCN KO mice (Figure 7E) and confirmed their expression in the VTA (Figure 7F). When these OCN KO mice were exposed to looming stimuli, however, no changes in cAMP or Ca^{2+} fluorescence were observed (Figures 7G and 7H, unpaired *t* test).

To further link the role of GPR37 to OCN-mediated cAMP regulation, we performed additional experiments in GPR37$^{-/-}$ mice. First, we measured baseline cAMP levels in VTA GABAergic neurons of GPR37$^{-/-}$ and WT mice and found that GPR37 deletion significantly elevated baseline cAMP levels compared with those in WT mice (Figures 7I and 7J, unpaired *t* test). We then tested whether restoring cAMP suppression rescues the impaired escape behavior of GPR37$^{-/-}$ mice by using 3′-phosphoadenosine-5′-phosphosulfate (PAPS, 0.3 mM), a cAMP blocker. Infusion of the PAPS into the VTA of GPR37$^{-/-}$ mice rescued their looming-evoked escape responses, indicating the necessity of cAMP reduction for rapid escape behavior (Figure 7K, unpaired *t* test).

Mechanistically, GPR37 activated by OCN reduces cAMP levels via a non-canonical Gi pathway, suppressing K2P13.1 channels encoded by KCNK13. This enhances excitability in VTA GABAergic neurons and facilitates rapid escape when visual threats are approaching (Figure 7L). The study underscores GPR37's role in modulating cAMP signaling and neuronal excitability in adaptive behaviors.

DISCUSSION

This study reveals an unforeseen mechanism in which bone-derived OCN permits rapid visual escape by activating the GPR37 receptor in a subset of VTA GABAergic neurons. OCN-GPR37 signaling enhances neuronal excitability via THIK-1 channel inhibition through a non-canonical pathway. These findings highlight OCN's role in modulating VTA circuits for survival-critical behaviors, uncovering a new axis of body-brain communication.

OCN plays a permissive role in visual escape by modulating neuronal excitability in the VTA

Our results demonstrate that OCN can directly increase neuronal excitability through the GPR37 receptor in a subset of GABAergic neurons by decreasing K^+ current via THIK-1 channels and reducing cAMP levels. THIK-1, belonging to the two-pore domain K^+ channel family, is responsible for modulating neuronal excitability by facilitating the efflux of potassium ions.[46–48] Notably, a previous study showed that rapid visual escape relies on instantaneous activation of VTA GABAergic neurons upon the presentation of looming stimuli.[12] Our new results indicated that OCN acts via GPR37 signaling to ensure that these neurons are in a state of readiness to rapidly respond to visual threats (Figure 4).

Notably, the way in which OCN increases neuronal excitability is distinguished from classical neuromodulators such as dopamine or choline, whose levels change acutely and dynamically upon environmental stimulation and animal behavior.[20,49,50] Given the fact that VTA neurons respond to looming stimuli within tens of milliseconds and that OCN is derived from the bone and enters the brain by passing through the BBB, OCN levels cannot increase before VTA neurons respond to looming. Thus, instead of playing an active role in modulating neuronal activity as classical neuromodulators, OCN plays a permissive role in maintaining heightened excitability of VTA GABAergic neuron subpopulations, making them ready to respond to sudden visual cues that reflect the rapid approach of a predator.

The above mechanism underscores the importance of situational adjustments and long-term preparatory states in maintaining adaptive responses to environmental challenges. OCN exerts a modulatory rather than a direct driving role in escape behavior. It optimizes the transformation of visual input to motor output by regulating processing at the VTA hub, which receives threat signals from the SC and relays them to downstream motor regions. The effect of OCN on VTA GABAergic neurons may tune their adaptive responses to various stimuli and conditions, including predator, prey, and stress stimuli, providing insights into the relationship between bone-brain interactions and mental health. Elevated KCNK13 levels in postmortem brains of Alzheimer's and Parkinson's patients[51] underscore the therapeutic potential of targeting KCNK13, as OCN does in specific VTA GABAergic subpopulations, highlighting the broader significance of our findings in understanding and treating neurological diseases. The identification of a specific KCNK13 blocker (CVN293) with potential anti-aging effects further underscores the translational relevance of this mechanism.

Dual GPCR receptor-potassium channel complexes mediate OCN's excitatory and inhibitory responses

Our snRNA-seq results showed that over 70% of VTA GABAergic neurons express both GABAergic and glutamatergic markers and potentially co-release these two neurotransmitters, highlighting the functional heterogeneity of VTA GABAergic neurons. Our findings demonstrate that GPR37 associates with the THIK-1 channel, exhibiting excitatory effects on OCN signaling, whereas GPR158 associates with G protein-gated inwardly rectifying potassium GIRK1 channel (also known as Kir3.1) encoded by the Kcnj3 gene, regulating the inhibitory effect on OCN. We identified GPR37's role in VTA GABA neurons, through which it facilitates the instant, energy-demanding escape via OCN signaling. The GPR158 receptor, which has recently been identified as a metabotropic glycine receptor, has been implicated as a mediator of OCN's regulation of hippocampus-dependent memory and stress-induced depression.[52–56] We found that GPR158 is expressed in virtually all GABAergic neurons, whereas GPR37 is only expressed in a subpopulation of these neurons. We demonstrate that the GPR158 receptor, known to associate with the RGS7-Gβ5 complex, interacts with the GIRK1 channel, which is distinctly expressed in VTA non-DA neurons, unlike the GIRK2/3 channels in VTA dopamine neurons.[57] Consistent with the modulation of GIRK channels by the RGS7-Gβ5 complex,[58,59] this GPR158-GIRK1 interaction leads to an inhibitory

response to OCN, in contrast to the regulation of GABAB receptor-GIRK2/3 coupling in VTA dopamine neurons by RGS2.[57] Our finding indicates that the OCN-GPR158 signaling pathway may serve as a critical hub, coordinating GIRK1 channel, may mediate OCN's long-term effects, enabling environmental recall and stress adaptation. Notably, our electrophysiology experiments suggest that the GPR37+ and GPR37− neurons are likely to be in two parallel circuits because the channel-specific blockers did not show cross effects. Thus, it is possible that OCN displays bidirectional control on the activity of distinct GABAergic circuits to differentially regulate distinct brain functions and behaviors. This dual-receptor mechanism—with GPR37/THIK-1 regulating acute neuronal excitability and GPR158/GIRK1 influencing tonic inhibition—provides a molecular framework for how bone-derived factors orchestrate both rapid behavioral states (fear and alertness) and long-term affective tuning (anxiety and depression).

Our finding that OCN bidirectionally modulates neuronal excitability adds to the growing body of evidence indicating that peripheral factors, such as glucocorticoids, insulin, and thyroid hormones, can regulate the activity of ion channels and neurotransmitter systems in the brain, thereby shaping behavioral and physiological responses to stress and environmental stimuli.[60–62] The intricate crosstalk between the periphery and the central nervous system, as exemplified by our findings on the role of bone-derived OCN in modulating neuronal excitability, underscores the importance of adopting a holistic perspective on body-brain interaction to fully elucidate the physiological mechanisms governing innate defensive behaviors and their dysregulation in fear and anxiety disorders.

Evolution of body-brain interactions for sensorimotor transformation

Our findings highlight an evolutionary strategy for integrating sensory and skeletal systems to optimize the threat response in vertebrates. The effect of OCN on VTA GABAergic circuits exemplifies the adaptive role of peripheral signals in shaping neural circuits and behavior.

Given the co-evolution of sensory and skeletal systems,[63,64] it is plausible that other bone-derived peripheral factors similarly influence sensory-motor transformations across neural circuits. OCN's regulation of potassium channels in VTA GABA neurons within the reward circuit reveals a molecular mechanism linking peripheral signals to central nervous system function and adaptive behaviors. The evolutionary conservation and duplication of the kcnk13 gene in teleosts underscore its critical role in the formation and patterning of both the skeletal system and the central nervous system.[65] Recent evidence further indicates that MN1-mediated co-development of the brain and skull reflects a deep evolutionary constraint, whereby behavior and neuroanatomy are hardwired by shared genetic programs.[66] Moreover, studies have revealed that vertebrates expanded their repertoire of anxiety-related genes during the water-to-land transition, likely to enhance alertness and promote survival.[67] Our findings highlight the potential of peripheral signals to modulate neural circuits and correct molecular dysfunctions, underscoring their relevance in disorders involving aberrant bone metabolism and altered neural interactions. They provide critical insights into the molecular basis of these cross-organ conditions, such as osteoporosis-linked depression and neurodegenerative diseases, paving the way for innovative therapeutic strategies grounded in brain-body interaction, cross-organ collaboration, and a holistic systems-based approach to treatment.[68–73]

Limitations of the study

Although we showed that VTA GABAergic neurons regulated by OCN-GPR37 mediate visual escape, the cell-type-specific downstream synaptic target neurons require further investigation. Additionally, the precise expression patterns of OCN receptors in other brain areas require further characterization. Integrating circuit level and spatial transcriptomic approaches can address these limitations, allowing a more comprehensive understanding of the role of OCN and its receptors in regulating neural circuit function.

RESOURCE AVAILABILITY

Lead contact

Requests for further information and resources should be directed to, and will be fulfilled by, the lead contact, Liping Wang (lp.wang@siat.ac.cn).

Materials availability

This study did not generate new reagents.

Data and code availability

- All data reported in this paper will be shared by the lead contact upon request.
- The codes and software used in the study have been deposited at https://github.com/xmliu1008/NEURON-VTA.
- Any additional information required to reanalyze the data reported in this paper is available from the lead contact upon request.

ACKNOWLEDGMENTS

We thank Dr. Helmut Kettenmann, Dr. Ming-Hu Han, and Dr. Guo-Qiang Bi for comments on our manuscript. This work was partially sponsored by STI2030-Major Projects-2022ZD0211700; National Natural Science Foundation of China (32230042 to Liping Wang, 32371069 to X. Liu, 32530045 to Liping Wang, and 32371019 to L.T.); Guangdong Basic and Applied Basic Research Foundation (2023B1515040009); Financial Support for Outstanding Talents Training Fund in Shenzhen (to Liping Wang); Shenzhen Science and Technology Program (KCXFZ20211020164543006, JCYJ20210324102201003, KQTD20210811090117032, and SYSPG20241211173950073); Guangdong Provincial Key Laboratory of Brain Connectome and Behavior, (2023B1212060055); the Financial Support for Outstanding Talents Training Fund in Shenzhen (Liping Wang); and the Ten Thousand Talent Program, the Chang Jiang Scholars Program, CAS Key Laboratory of Brain Connectome and Manipulation (2019DP173024), and National Key R&D Program of China to L.T. (2022YFA1105503). We sincerely thank the Shenzhen Brain Science Infrastructure for their essential technical support in this study.

AUTHOR CONTRIBUTIONS

Conceptualization, X. Li, X. Liu, and Liping Wang; methodology, X. Liu, X. Li, L.T., S.W., J.L., X.G., and Liping Wang; investigation, X. Liu, J.L., S.W., L.T., X.G., Lina Wang, B.F., L.Y., and Z.Q.; writing – original draft, X. Liu; writing – review and editing, X. Liu, L.T., X. Li, S.W., and Liping Wang; funding acquisition, Liping Wang, X. Liu, X. Li, and L.T.; resources, Liping Wang, X. Liu, and X. Li; and supervision, X. Liu, X. Li, Liping Wang, and L.T.

DECLARATION OF INTERESTS

Liping Wang serves on *Neuron*'s scientific advisory board.

STAR★METHODS

Detailed methods are provided in the online version of this paper and include the following:

- KEY RESOURCES TABLE
- EXPERIMENTAL MODEL AND STUDY PARTICIPANT DETAILS
  - Male mice
  - Viruses
- METHOD DETAILS
  - Stereotaxic Surgery and virus injection
  - Looming test
  - Looming Behavioral analysis
  - Fiber photometry
  - 3D behavior collection and analysis
  - Serum OCN detection following acute stimuli
  - Serum Osteocalcin Measurement
  - Bioinformatic analysis
- QUANTIFICATION AND STATISTICAL ANALYSIS

SUPPLEMENTAL INFORMATION

Supplemental information can be found online at https://doi.org/10.1016/j.neuron.2025.12.048.

Received: April 10, 2025
Revised: November 8, 2025
Accepted: December 27, 2025

REFERENCES

1. Romer, A.S. (1933). Eurypterid Influence on Vertebrate History. https://doi.org/10.1038/s41583-023-00736-3.
2. Tseng, Y.-T., Schaefke, B., Wei, P., and Wang, L. (2023). Defensive responses: behaviour, the brain and the body. Nat. Rev. Neurosci. *24*, 655–671. https://doi.org/10.1038/s41583-023-00736-3.
3. LeDoux, J. (2012). Rethinking the emotional brain. Neuron *73*, 653–676. https://doi.org/10.1016/j.neuron.2012.02.004.
4. LeDoux, J., and Daw, N.D. (2018). Surviving threats: neural circuit and computational implications of a new taxonomy of defensive behaviour. Nat. Rev. Neurosci. *19*, 269–282. https://doi.org/10.1038/nrn.2018.22.
5. Anderson, D.J., and Adolphs, R. (2014). A framework for studying emotions across species. Cell *157*, 187–200. https://doi.org/10.1016/j.cell.2014.03.003.
6. Gross, C.T., and Canteras, N.S. (2012). The many paths to fear. Nat. Rev. Neurosci. *13*, 651–658. https://doi.org/10.1038/nrn3301.
7. Yilmaz, M., and Meister, M. (2013). Rapid innate defensive responses of mice to looming visual stimuli. Curr. Biol. *23*, 2011–2015. https://doi.org/10.1016/j.cub.2013.08.015.
8. Wei, P., Liu, N., Zhang, Z., Liu, X., Tang, Y., He, X., Wu, B., Zhou, Z., Liu, Y., Li, J., et al. (2015). Processing of visually evoked innate fear by a non-canonical thalamic pathway. Nat. Commun. *6*, 6756. https://doi.org/10.1038/ncomms7756.
9. Shang, C., Chen, Z., Liu, A., Li, Y., Zhang, J., Qu, B., Yan, F., Zhang, Y., Liu, W., Liu, Z., et al. (2018). Divergent midbrain circuits orchestrate escape and freezing responses to looming stimuli in mice. Nat. Commun. *9*, 1232. https://doi.org/10.1038/s41467-018-03580-7.
10. Salay, L.D., Ishiko, N., and Huberman, A.D. (2018). A midline thalamic circuit determines reactions to visual threat. Nature *557*, 183–189. https://doi.org/10.1038/s41586-018-0078-2.
11. Evans, D.A., Stempel, A.V., Vale, R., Ruehle, S., Lefler, Y., and Branco, T. (2018). A synaptic threshold mechanism for computing escape decisions. Nature *558*, 590–594. https://doi.org/10.1038/s41586-018-0244-6.
12. Zhou, Z., Liu, X., Chen, S., Zhang, Z., Liu, Y., Montardy, Q., Tang, Y., Wei, P., Liu, N., Li, L., et al. (2019). A VTA GABAergic Neural Circuit Mediates Visually Evoked Innate Defensive Responses. Neuron *103*, 473–488.e6. https://doi.org/10.1016/j.neuron.2019.05.027.
13. Li, L., Feng, X., Zhou, Z., Zhang, H., Shi, Q., Lei, Z., Shen, P., Yang, Q., Zhao, B., Chen, S., et al. (2018). Stress Accelerates Defensive Responses to Looming in Mice and Involves a Locus Coeruleus-Superior Colliculus Projection. Curr. Biol. *28*, 859–871.e5. https://doi.org/10.1016/j.cub.2018.02.005.
14. Schiff, W., Caviness, J.A., and Gibson, J.J. (1962). Persistent Fear Responses in Rhesus Monkeys to the Optical Stimulus of "Looming.". Science *136*, 982–983. https://doi.org/10.1126/science.136.3520.982.
15. Huang, L., Yuan, T., Tan, M., Xi, Y., Hu, Y., Tao, Q., Zhao, Z., Zheng, J., Han, Y., Xu, F., et al. (2017). A retinoraphe projection regulates serotonergic activity and looming-evoked defensive behaviour. Nat. Commun. *8*, 14908. https://doi.org/10.1038/ncomms14908.
16. Schultz, W., Dayan, P., and Montague, P.R. (1997). A neural substrate of prediction and reward. Science *275*, 1593–1599. https://doi.org/10.1126/science.275.5306.1593.
17. Russo, S.J., and Nestler, E.J. (2013). The brain reward circuitry in mood disorders. Nat. Rev. Neurosci. *14*, 609–625. https://doi.org/10.1038/nrn3381.
18. Morales, M., and Margolis, E.B. (2017). Ventral tegmental area: cellular heterogeneity, connectivity and behaviour. Nat. Rev. Neurosci. *18*, 73–85. https://doi.org/10.1038/nrn.2016.165.
19. Lammel, S., Lim, B.K., Ran, C., Huang, K.W., Betley, M.J., Tye, K.M., Deisseroth, K., and Malenka, R.C. (2012). Input-specific control of reward and aversion in the ventral tegmental area. Nature *491*, 212–217. https://doi.org/10.1038/nature11527.
20. Bromberg-Martin, E.S., Matsumoto, M., and Hikosaka, O. (2010). Dopamine in motivational control: rewarding, aversive, and alerting. Neuron *68*, 815–834. https://doi.org/10.1016/j.neuron.2010.11.022.
21. Barbano, M.F., Wang, H.L., Zhang, S., Miranda-Barrientos, J., Estrin, D.J., Figueroa-González, A., Liu, B., Barker, D.J., and Morales, M. (2020). VTA Glutamatergic Neurons Mediate Innate Defensive Behaviors. Neuron *107*, 368–382.e8. https://doi.org/10.1016/j.neuron.2020.04.024.
22. Hsueh, B., Chen, R., Jo, Y.J., Tang, D., Raffiee, M., Kim, Y.S., Inoue, M., Randles, S., Ramakrishnan, C., Patel, S., et al. (2023). Cardiogenic control of affective behavioural state. Nature *615*, 292–299. https://doi.org/10.1038/s41586-023-05748-8.
23. Signoret-Genest, J., Schukraft, N., L Reis, S., Segebarth, D., Deisseroth, K., and Tovote, P. (2023). Integrated cardio-behavioral responses to threat define defensive states. Nat. Neurosci. *26*, 447–457. https://doi.org/10.1038/s41593-022-01252-w.
24. Bin, N.-R., Prescott, S.L., Horio, N., Wang, Y., Chiu, I.M., and Liberles, S.D. (2023). An airway-to-brain sensory pathway mediates influenza-induced sickness. Nature *615*, 660–667. https://doi.org/10.1038/s41586-023-05796-0.
25. Gannot, N., Li, X., Phillips, C.D., Ozel, A.B., Uchima Koecklin, K.H., Lloyd, J.P., Zhang, L., Emery, K., Stern, T., Li, J.Z., et al. (2024). A vagal–brainstem interoceptive circuit for cough-like defensive behaviors in mice. Nat. Neurosci. *27*, 1734–1744. https://doi.org/10.1038/s41593-024-01712-5.
26. Oury, F., Khrimian, L., Denny, C.A., Gardin, A., Chamouni, A., Goeden, N., Huang, Y.Y., Lee, H., Srinivas, P., Gao, X.B., et al. (2013). XMaternal and offspring pools of osteocalcin influence brain development and functions. Cell *155*, 228–241. https://doi.org/10.1016/j.cell.2013.08.042.
27. Karsenty, G., and Oury, F. (2012). Biology without walls: The novel endocrinology of bone. Annu. Rev. Physiol. *74*, 87–105. https://doi.org/10.1146/annurev-physiol-020911-153233.

28. Karsenty, G. (2023). Osteocalcin: A Multifaceted Bone-Derived Hormone. Annu. Rev. Nutr. *43*, 55–71. https://doi.org/10.1146/annurev-nutr-061121-091348.

29. Obri, A., Khrimian, L., Karsenty, G., and Oury, F. (2018). Osteocalcin in the brain: from embryonic development to age-related decline in cognition. Nat. Rev. Endocrinol. *14*, 174–182. https://doi.org/10.1038/nrendo.2017.181.

30. Berger, J.M., Singh, P., Khrimian, L., Morgan, D.A., Chowdhury, S., Arteaga-Solis, E., Horvath, T.L., Domingos, A.I., Marsland, A.L., Yadav, V.K., et al. (2019). Mediation of the Acute Stress Response by the Skeleton. Cell Metab. *30*, 890–902.e8. https://doi.org/10.1016/j.cmet.2019.08.012.

31. Mosialou, I., Shikhel, S., Liu, J.M., Maurizi, A., Luo, N., He, Z., Huang, Y., Zong, H., Friedman, R.A., Barasch, J., et al. (2017). MC4R-dependent suppression of appetite by bone-derived lipocalin 2. Nature *543*, 385–390. https://doi.org/10.1038/nature21697.

32. Bhattacharyya, N., Chong, W.H., Gafni, R.I., and Collins, M.T. (2012). Fibroblast growth factor 23: state of the field and future directions. Trends Endocrinol. Metab. *23*, 610–618. https://doi.org/10.1016/j.tem.2012.07.002.

33. Ferron, M., Wei, J., Yoshizawa, T., Del Fattore, A., DePinho, R.A., Teti, A., Ducy, P., and Karsenty, G. (2010). Insulin Signaling in Osteoblasts Integrates Bone Remodeling and Energy Metabolism. Cell *142*, 296–308. https://doi.org/10.1016/j.cell.2010.06.003.

34. Qian, Z., Li, H., Yang, H., Yang, Q., Lu, Z., Wang, L., Chen, Y., and Li, X. (2021). Osteocalcin attenuates oligodendrocyte differentiation and myelination via GPR37 signaling in the mouse brain. Sci. Adv. *7*, eabi5811. https://doi.org/10.1126/sciadv.abi5811.

35. Dimidschstein, J., Chen, Q., Tremblay, R., Rogers, S.L., Saldi, G.A., Guo, L., Xu, Q., Liu, R., Lu, C., Chu, J., et al. (2016). A viral strategy for targeting and manipulating interneurons across vertebrate species. Nat. Neurosci. *19*, 1743–1749. https://doi.org/10.1038/nn.4430.

36. Liu, X., Lai, J., Han, C., Zhong, H., Huang, K., Liu, Y., Zhu, X., Wei, P., Tan, L., Xu, F., et al. (2025). Neural circuit underlying individual differences in visual escape habituation. Neuron *113*, 2344–2357.e5. https://doi.org/10.1016/j.neuron.2025.04.018.

37. Aceto, G., Nardella, L., Nanni, S., Pecci, V., Bertozzi, A., Nutarelli, S., Viscomi, M.T., Colussi, C., D'Ascenzo, M., and Grassi, C. (2024). Glycine-induced activation of GPR158 increases the intrinsic excitability of medium spiny neurons in the nucleus accumbens. Cell. Mol. Life Sci. *81*, 268. https://doi.org/10.1007/s00018-024-05260-w.

38. Wolock, S.L., Lopez, R., and Klein, A.M. (2019). Scrublet: Computational Identification of Cell Doublets in Single-Cell Transcriptomic Data. Cell Syst. *8*, 281–291.e9. https://doi.org/10.1016/j.cels.2018.11.005.

39. Bürli, R.W., Doyle, K.J., Dickson, L., Rowland, A., Matthews, K., Stott, A.J., Teall, M., Ossola, B., Russell, S.G., Harvey, J.R.M., et al. (2024). Discovery of CVN293, a Brain Permeable KCNK13 (THIK-1) Inhibitor Suitable for Clinical Assessment. ACS Med. Chem. Lett. *15*, 646–652. https://doi.org/10.1021/acsmedchemlett.4c00035.

40. Gonzalez, J.C., Epps, S.A., Markwardt, S.J., Wadiche, J.I., and Overstreet-Wadiche, L. (2018). Constitutive and Synaptic Activation of GIRK Channels Differentiates Mature and Newborn Dentate Granule Cells. J. Neurosci. *38*, 6513–6526. https://doi.org/10.1523/JNEUROSCI.0674-18.2018.

41. Blumenthal, E.M., and Kaczmarek, L.K. (1992). Modulation by cAMP of a slowly activating potassium channel expressed in Xenopus oocytes. J. Neurosci. *12*, 290–296. https://doi.org/10.1523/JNEUROSCI.12-01-00290.1992.

42. Walsh, K.B., and Kass, R.S. (1988). Regulation of a Heart Potassium Channel by Protein Kinase A and C. Science *242*, 67–69. https://doi.org/10.1126/science.2845575.

43. van der Horst, J., Greenwood, I.A., and Jepps, T.A. (2020). Cyclic AMP-Dependent Regulation of Kv7 Voltage-Gated Potassium Channels. Front. Physiol. *11*, 727. https://doi.org/10.3389/fphys.2020.00727.

44. Kang, G., Chepurny, O.G., Malester, B., Rindler, M.J., Rehmann, H., Bos, J.L., Schwede, F., Coetzee, W.A., and Holz, G.G. (2006). cAMP sensor Epac as a determinant of ATP-sensitive potassium channel activity in human pancreatic β cells and rat INS-1 cells. J. Physiol. *573*, 595–609. https://doi.org/10.1113/jphysiol.2006.107391.

45. Meyer, R.C., Giddens, M.M., Schaefer, S.A., and Hall, R.A. (2013). GPR37 and GPR37L1 are receptors for the neuroprotective and glioprotective factors prosaptide and prosaposin. Proc. Natl. Acad. Sci. USA *110*, 9529–9534. https://doi.org/10.1073/pnas.1219004110.

46. Goldstein, S.A.N., Bockenhauer, D., O'Kelly, I., and Zilberberg, N. (2001). Potassium leak channels and the KCNK family of two-p-domain subunits. Nat. Rev. Neurosci. *2*, 175–184. https://doi.org/10.1038/35058574.

47. Schewe, M., Nematian-Ardestani, E., Sun, H., Musinszki, M., Cordeiro, S., Bucci, G., de Groot, B.L., Tucker, S.J., Rapedius, M., and Baukrowitz, T. (2016). A Non-canonical Voltage-Sensing Mechanism Controls Gating in K2P K+ Channels. Cell *164*, 937–949. https://doi.org/10.1016/j.cell.2016.02.002.

48. Rajan, S., Wischmeyer, E., Karschin, C., Preisig-Müller, R., Grzeschik, K.H., Daut, J., Karschin, A., and Derst, C. (2001). THIK-1 and THIK-2, a Novel Subfamily of Tandem Pore Domain K+ Channels. J. Biol. Chem. *276*, 7302–7311. https://doi.org/10.1074/jbc.M008985200.

49. Hangya, B., Ranade, S.P., Lorenc, M., and Kepecs, A. (2015). Central Cholinergic Neurons Are Rapidly Recruited by Reinforcement Feedback. Cell *162*, 1155–1168. https://doi.org/10.1016/j.cell.2015.07.057.

50. Motelow, J.E., Li, W., Zhan, Q., Mishra, A.M., Sachdev, R.N.S., Liu, G., Gummadavelli, A., Zayyad, Z., Lee, H.S., Chu, V., et al. (2015). Decreased Subcortical Cholinergic Arousal in Focal Seizures. Neuron *85*, 561–572. https://doi.org/10.1016/j.neuron.2014.12.058.

51. Tang, H., Sun, Y., Fachim, H.A., Cheung, T.K.D., Reynolds, G.P., and Harte, M.K. (2023). Elevated Expression of Two Pore Potassium Channel THIK-1 in Alzheimer's Disease: An Inflammatory Mechanism. J. Alzheimers Dis. *95*, 1757–1769. https://doi.org/10.3233/JAD-230616.

52. Laboute, T., Zucca, S., Holcomb, M., Patil, D.N., Garza, C., Wheatley, B.A., Roy, R.N., Forli, S., and Martemyanov, K.A. (2023). Orphan receptor GPR158 serves as a metabotropic glycine receptor: mGlyR. Science *379*, 1352–1358. https://doi.org/10.1126/science.add7150.

53. Khrimian, L., Obri, A., Ramos-Brossier, M., Rousseaud, A., Moriceau, S., Nicot, A.S., Mera, P., Kosmidis, S., Karnavas, T., Saudou, F., et al. (2017). Gpr158 mediates osteocalcin's regulation of cognition. J. Exp. Med. *214*, 2859–2873. https://doi.org/10.1084/jem.20171320.

54. Sutton, L.P., Orlandi, C., Song, C., Oh, W.C., Muntean, B.S., Xie, K., Filippini, A., Xie, X., Satterfield, R., Yaeger, J.D.W., et al. (2018). Orphan receptor GPR158 controls stress-induced depression. eLife *7*, e33273. https://doi.org/10.7554/eLife.33273.

55. Kosmidis, S., Polyzos, A., Harvey, L., Youssef, M., Denny, C.A., Dranovsky, A., and Kandel, E.R. (2018). RbAp48 Protein Is a Critical Component of GPR158/OCN Signaling and Ameliorates Age-Related Memory Loss. Cell Rep. *25*, 959–973.e6. https://doi.org/10.1016/j.celrep.2018.09.077.

56. Ertuğrul Uygun, H.D. (2024). Use of osteocalcin-specific Gpr158 protein in biosensor technology for osteocalcin detection. Chem. Pap. *78*, 5577–5583. https://doi.org/10.1007/s11696-024-03500-8.

57. Labouèbe, G., Lomazzi, M., Cruz, H.G., Creton, C., Luján, R., Li, M., Yanagawa, Y., Obata, K., Watanabe, M., Wickman, K., et al. (2007). RGS2 modulates coupling between GABAB receptors and GIRK channels in dopamine neurons of the ventral tegmental area. Nat. Neurosci. *10*, 1559–1568. https://doi.org/10.1038/nn2006.

58. Lomazzi, M., Slesinger, P.A., and Lüscher, C. (2008). Addictive drugs modulate GIRK-channel signaling by regulating RGS proteins. Trends Pharmacol. Sci. *29*, 544–549. https://doi.org/10.1016/j.tips.2008.07.011.

59. Lüscher, C., and Slesinger, P.A. (2010). Emerging roles for G protein-gated inwardly rectifying potassium (GIRK) channels in health and disease. Nat. Rev. Neurosci. *11*, 301–315. https://doi.org/10.1038/nrn2834.

60. Imaki, T., Xiao-Quan, W., Shibasaki, T., Yamada, K., Harada, S., Chikada, N., Naruse, M., and Demura, H. (1995). Stress-induced activation of neuronal activity and corticotropin-releasing factor gene expression in the paraventricular nucleus is modulated by glucocorticoids in rats. J. Clin. Investig. *96*, 231–238. https://doi.org/10.1172/JCI118026.

61. Nishijima, T., Piriz, J., Duflot, S., Fernandez, A.M., Gaitan, G., Gomez-Pinedo, U., Verdugo, J.M.G., Leroy, F., Soya, H., Nuñez, A., et al. (2010). Neuronal Activity Drives Localized Blood-Brain-Barrier Transport of Serum Insulin-like Growth Factor-I into the CNS. Neuron *67*, 834–846. https://doi.org/10.1016/j.neuron.2010.08.007.

62. Caria, M.A., Dratman, M.B., Kow, L.M., Mameli, O., and Pavlides, C. (2009). Thyroid Hormone Action: Nongenomic Modulation of Neuronal Excitability in the Hippocampus. J. Neuroendocrinol. *21*, 98–107. https://doi.org/10.1111/j.1365-2826.2008.01813.x.

63. Shimeld, S.M., and Holland, P.W.H. (2000). Vertebrate innovations. Proc. Natl. Acad. Sci. USA *97*, 4449–4452. https://doi.org/10.1073/pnas.97.9.4449.

64. Green, S.A., Simoes-Costa, M., and Bronner, M.E. (2015). Evolution of vertebrates as viewed from the crest. Nature *520*, 474–482. https://doi.org/10.1038/nature14436.

65. Park, S.J., Silic, M.R., Staab, P.L., Chen, J., Zackschewski, E.L., and Zhang, G. (2024 Aug). Evolution of two-pore domain potassium channels and their gene expression in zebrafish embryos. Dev. Dyn. *253*, 722–749. https://doi.org/10.1002/dvdy.690.

66. Escamilla-Vega, E., Seton, L.W.G., Kyomen, S., Murillo-Rincón, A.P., Petersen, J., Tautz, D., and Kaucká, M. (2025 Jun 3). Evolution of the essential gene MN1 during the macroevolutionary transition toward patterning the vertebrate hindbrain. Proc. Natl. Acad. Sci. USA *122*, e2416061122. https://doi.org/10.1073/pnas.2416061122.

67. Wang, K., Wang, J., Zhu, C., Yang, L., Ren, Y., Ruan, J., Fan, G., Hu, J., Xu, W., Bi, X., et al. (2021 Mar 4). African lungfish genome sheds light on the vertebrate water-to-land transition. Cell *184*, 1362–1376.e18. https://doi.org/10.1016/j.cell.2021.01.047.

68. Gordon, J.A., Dzirasa, K., and Petzschner, F.H. (2024). The neuroscience of mental illness: Building toward the future. Cell *187*, 5858–5870. https://doi.org/10.1016/j.cell.2024.09.028.

69. Lv, X., Gao, F., and Cao, X. (2022). Skeletal interoception in bone homeostasis and pain. Cell Metab. *34*, 1914–1931. https://doi.org/10.1016/j.cmet.2022.09.025.

70. Karsenty, G., and Khosla, S. (2022). The crosstalk between bone remodeling and energy metabolism: A translational perspective. Cell Metab. *34*, 805–817. https://doi.org/10.1016/j.cmet.2022.04.010.

71. Zaidi, M., Zaidi, S., and Yuen, T. (2024). Understanding osteokine biology. Cell Metab. *36*, 888–890. https://doi.org/10.1016/j.cmet.2024.04.008.

72. Liu, Z.T., Liu, M.H., Xiong, Y., Wang, Y.J., and Bu, X.L. (2024). Crosstalk between bone and brain in Alzheimer's disease: Mechanisms, applications, and perspectives. Alzheimers. Dement. *20*, 5720–5739. https://doi.org/10.1002/alz.13864.

73. Li, R., Miao, Z., Liu, Y., Chen, X., Wang, H., Su, J., and Chen, J. (2024). The Brain-Gut-Bone Axis in Neurodegenerative Diseases: Insights, Challenges, and Future Prospects. Adv. Sci. *11*, e2307971. https://doi.org/10.1002/advs.202307971.

74. Wolf, F.A., Hamey, F.K., Plass, M., Solana, J., Dahlin, J.S., Göttgens, B., Rajewsky, N., Simon, L., and Theis, F.J. (2019). PAGA: graph abstraction reconciles clustering with trajectory inference through a topology preserving map of single cells. Genome Biol. *20*, 59. https://doi.org/10.1186/s13059-019-1663-x.

75. Korsunsky, I., Millard, N., Fan, J., Slowikowski, K., Zhang, F., Wei, K., Baglaenko, Y., Brenner, M., Loh, P.R., and Raychaudhuri, S. (2019). Fast, sensitive and accurate integration of single-cell data with Harmony. Nat. Methods *16*, 1289–1296. https://doi.org/10.1038/s41592-019-0619-0.

76. Tseng, Y.T., Zhao, B., Chen, S., Ye, J., Liu, J., Liang, L., Ding, H., Schaefke, B., Yang, Q., Wang, L., et al. (2022). The subthalamic corticotropin-releasing hormone neurons mediate adaptive REM-sleep responses to threat. Neuron *110*, 1223–1239.e8. https://doi.org/10.1016/j.neuron.2021.12.033.

77. Zhong, H., Lu, K., Wang, L., Wang, W., Wei, P., and Liu, X. (2025). Subtle behavioral alterations in the spontaneous behaviors of MPTP mouse model of Parkinson's disease. Transl. Psychiatry *15*, 119. https://doi.org/10.1038/s41398-025-03312-8.

78. Huang, K., Han, Y., Chen, K., Pan, H., Zhao, G., Yi, W., Li, X., Liu, S., Wei, P., and Wang, L. (2021). A hierarchical 3D-motion learning framework for animal spontaneous behavior mapping. Nat. Commun. *12*, 2784. https://doi.org/10.1038/s41467-021-22970-y.

79. Cheng, S., Butrus, S., Tan, L., Xu, R., Sagireddy, S., Trachtenberg, J.T., Shekhar, K., and Zipursky, S.L. (2022). Vision-dependent specification of cell types and function in the developing cortex. Cell *185*, 311–327.e24. https://doi.org/10.1016/j.cell.2021.12.022.

80. Chen, G., Lai, S., Jiang, S., Li, F., Sun, K., Wu, X., Zhou, K., Liu, Y., Deng, X., Chen, Z., et al. (2024). Cellular and circuit architecture of the lateral septum for reward processing. Neuron *112*, 2783–2798.e9. https://doi.org/10.1016/j.neuron.2024.06.004.

81. Wu, X., Xu, W., Deng, L., Li, Y., Wang, Z., Sun, L., Gao, A., Wang, H., Yang, X., Wu, C., et al. (2024). Spatial multi-omics at subcellular resolution via high-throughput in situ pairwise sequencing. Nat. Biomed. Eng. *8*, 872–889. https://doi.org/10.1038/s41551-024-01205-7.

Please cite this article in press as: Liu et al., A bone-derived hormone permits rapid visual escape via GPR37 receptor in a subpopulation of VTA GABAergic neurons, Neuron (2025), https://doi.org/10.1016/j.neuron.2025.12.048

STAR★METHODS

KEY RESOURCES TABLE

REAGENT or RESOURCE	SOURCE	IDENTIFIER
Antibodies		
DAPI	Thermofisher	Cat#62248; RRID:AB_2313773
Mouse anti-TH	Millipore	Cat#MAB318; RRID:AB_2201528
Mouse anti-GAD67	Millipore	Cat#MAB5406; RRID:AB_2938602
Rabbit anti-GPR37	Cell Signaling Technology	Cat#64407; RRID:AB_2799658
Goat anti-mouse IgG(H+L) alexa fluor@594-conjugated affinipure	Jackson immuno research	Cat#115-585-003; RRID:AB_2338871
Goat anti-rabbit alexa fluor@647-conjugated affinipure fab fragment	Abcam	Cat#ab150079; RRID:AB_2722623
Mouse anti-GPR37 (Pael-R (G-6))	Santa Cruz Biotechnology, Inc.	Cat#sc-390110; RRID:AB_2313773
KCNK13 Polyclonal Antibody	Thermofisher	Cat# PA5-50434; RRID:AB_2635887
GAPDH Mouse Monoclonal Antibody	Beyotime	Cat# AF2819; RRID:AB_2313773
Bacterial and virus strains		
Lenti-GPR37–GFP	Liping Wang's Lab at the CAS	N/A
LV-CMV–GFP	BrainCase Co., Ltd., China	N/A
AAV2/9-Dlx5/6-cre-GFP	Liping Wang's Lab at the CAS	N/A
AAV2/9-Dlx5/6-GFP	BrainCase Co., Ltd.,China	N/A
AAV2/9-mTH- Cre-GFP	BrainCase Co., Ltd.,China	N/A
AAV2/9-CaMKIIα-GFP	BrainCase Co., Ltd.,China	N/A
AAV2/9-CaMKIIα-Cre-GFP	BrainCase Co., Ltd.,China	N/A
AAV2/9-mTH-GFP	BrainCase Co., Ltd.,China	N/A
AAV2/9-Ef1α-DIO-mCherry	Liping Wang's Lab at the CAS	N/A
AAV2/9-Ef1α-DIO-GFP	Liping Wang's Lab at the CAS	N/A
rAAV9-mDIX-GFlamp2-WPRE-pA	BrainVTA Co., Ltd., China	N/A
rAAV9-hsyn-DIO-GFlamp2	BrainVTA Co., Ltd., China	N/A
rAAV9- Dlx-NES-Som aFRCaMPi	BrainCase Co., Ltd., China	N/A
rAAV9- hSy-NES-SomaFRCaMPi	BrainCase Co., Ltd., China	N/A
Deposited data		
Computation code of https://github.com/xmliu1008/NEURON-VTA	Github	https://github.com/xmliu1008/NEURON-VTA
Chemicals, peptides, and recombinant proteins		
DAPI	Thermofisher	Cat#62248
Clozapine-N-Oxide	Apexbio	Cat# A3317
Biotin Protein Labeling Kit	Roche	Cat#11418165001
Mouse Glu- Osteocalcin High Sensitive EIA Kit	Takara	Cat#MK129
Osteocalcin	Invitrogen	Cat#PA5-86886
3'-phosphoadenosine-5'-phosphosulfate (PAPS)	Merck	Cat#A1651
CVN293	MedChemExpress	HY-158155
Tertiapin-Q	MedChemExpress	HY-P1275
NPPB	GLPBIO	GC14268
Cadmium Chloride	Aladdin	C116344-50g
TTX	Biogradetech	BGT-CHM-430
DL-AP5	Abcam	Ab120004

(*Continued on next page*)

Continued

REAGENT or RESOURCE	SOURCE	IDENTIFIER
CNQX	Tocris	Cat.No.1045/1
Bicuculline	Tocris	Cat.No.0130/50
Experimental models: Organisms/strains		
C57BL/6J mice	Zhejiang Vital River Laboratory Animal Technology Co., Ltd., Zhejiang, China	N/A
DAT-ires-Cre mice; Slc6a3tm1.1(cre)Bkmn/J	The Jackson Laboratory	Stock No: 006660
GAD2-ires-Cre mice; Gad2tm2(cre)Zjh/J	The Jackson Laboratory	Stock No: 010802
VGluT2-ires-Cre mice; Slc17a6tm2(cre)Lowl/J	The Jackson Laboratory	Stock No: 016963
OCN-/- mice	Shanghai Model Organisms Co., Ltd (Shanghai, China)	N/A
B6.129P2-Gpr37tm1Dgen/J, GPR37-/- mice	The Jackson Laboratory	Stock No: #005806
Gpr158-/- mice	Shanghai Model Organisms Co., Ltd (Shanghai, China)	N/A
GPR37 LoxP/ LoxP mice	Shanghai Model Organisms Co., Ltd (Shanghai, China)	N/A
KCNK13 LoxP/ LoxP mice	GemPharmatech Co., Ltd.	N/A
Software and algorithms		
GraphPad Prism 9.0	GraphPad Software Inc	http://www.graphpad.com/scientific-software/prism/
Cell Ranger 7.2.0	10X Genomics	www.support.10xgenomics.com/single-cell-gene-expression/software/overview/welcome
Python 3.11.7	Python	https://www.python.org/
SCANPY 1.10.1	Wolf et al., 2019[74]	https://pypi.org/project/scanpy/
Scikit-learn 1.2.2	Scikit-learn	https://pypi.org/project/scikit-learn/
Harmony 0.0.9	Korsunsky et al.[75]	https://github.com/ immunogenomics/harmony
ImageJ	NIH	https://imagej.nih.gov/ij/
Image Pro-plus	Media Cybernetics, Inc	http://en.freedownloadmanager.org/Windows-PC/Image-Pro-Plus.html
Zen softwares	Zeiss	http://www.zeiss.com/corporate/en_de/global/home.html
Adobe Photoshop	Adobe Systems Inc	https://www.adobe.com/
Adobe Premiere	Adobe Systems Inc	https://www.adobe.com/
pClamp 10	Axon instruments	https://www.moleculardevices.com/
RStudio	Posit PBC	https://posit.co/downloads/
Matlab	MathWorks, Inc	https://www.mathworks.com/company.html
BehaviorAtlas Analyzer 1.0	Shenzhen Bayone BioTechCo, Ltd., Shenzhen, China	https://behavioratlas.tech/
BehaviorAtlas Capture 1.0	Shenzhen Bayone BioTech Co., Ltd., Shenzhen, China	https://behavioratlas.tech/

EXPERIMENTAL MODEL AND STUDY PARTICIPANT DETAILS

Male mice

All experimental procedures were approved by the Animal Care and Use Committees at the Shenzhen Institute of Advanced Technology (SIAT), Chinese Academy of Sciences (CAS). Adult (6 to 8 weeks-old) male C57BL/6 (Zhejiang Vital River Laboratory Animal Technology Co., Ltd., Zhejiang, China), GAD2-*ires*-Cre (Jax No. #010802) mice, DAT-*ires*-Cre (Jax No. #006660), VGluT2-ires-Cre

(Jax No. #016963), GPR37$^{-/-}$ mice (B6.129P2-Gpr37tm1Dgen/J, Jax No. #005806) were used in this study. The OCN$^{-/-}$ and GPR37 $^{LoxP/LoxP}$ mice were generated using CRISPR- Cas9 technique by Shanghai Model Organisms Co., Ltd (Shanghai, China). GPR37cKO and control animals (GPR37$^{flox/flox}$) were obtained from crossed between DAT-*ires*-Cre animals; GPR37flx/flx and DAT-*ires*-Cre animals. All animals were housed at 22–25 °C on a circadian cycle of 12-hour light and 12-hour dark with ad-libitum access to food and water. All mice were maintained in specific pathogen-free (SPF) conditions and were confirmed free of *Salmonella* spp., *Mycoplasma* spp., *Corynebacterium kutscheri*, Tyzzer's organism, *Pasteurella pneumotropica*, *Klebsiella pneumoniae*, *Pseudomonas aeruginosa*, Mouse Hepatitis Virus (MHV), Sendai Virus (SeV), Pneumonia Virus of Mice (PVM), Minute Virus of Mice (MVM), Reovirus type 3 (Reo-3), Ciliates, All Helminths, Flagellates, Toxoplasma gondii and Ectoparasites according to National standard for pathogen detection of SPF-grade laboratory animals (GB14922-2022). The mice used in this study were naive to all prior experimental procedures, with no involvement in any previous studies, and were undergoing drug or behavioral testing for the first time.

Viruses

For specific VTA recovery GPR37, we used plasmids for lenti-viruses encoding GPR37–GFP, were packaged by Liping Wang Lab, Shenzhen. Viral vector titers were in the range of 3-6x10^{12} genome copies per ml (gc)/mL.

For specific neuron types knock out GPR37 receptor and anatomical labeling, AAV2/9 virus encoding mTH-cre-EGFP and the control virus mTH-EGFP were all packaged by BrainCase Co., Ltd., Shenzhen, and Dlx5/6-cre-GFP and the control virusDlx5/6-GFP, Ef1α-DIO-mcherry were all packaged by Liping Wang Lab, Shenzhen. Adeno-associated were purified and concentrated to titers at approximately 3×10^{12} v.g/ml and 1×10^{9} pfu/ml, respectively.

For monitor dynamic signaling in specific neural subtypes, we implemented genetically encoded sensors delivered via rAAV vectors. cAMP dynamics were recorded using rAAV9-hsyn-DIO-GFlamp2 and rAAV9-mDIX-GFlamp2-WPRE-pA (BrainVTA Co., Ltd.), while calcium transients were measured with rAAV9-Dlx-NES-SomaFRCaMPi (GABAergic-specific) and rAAV9-hSy-NES-SomaFRCaMPi (pan-neuronal) (BrainCase Co., Ltd.). All viruses were purified to titers $\geq3\times10^{12}$ vg/ml.

METHOD DETAILS

Stereotaxic Surgery and virus injection

Stereotaxic surgeries were performed as described previously[12]. Briefly, Animals were anesthetized with pentobarbital (i.p., 80 mg/kg) and then positioned in a stereotaxic apparatus (RWD, China). Injections were conducted by a syringe (Hamilton #65460-05, 10ul) under the control of a micro syringe pump (KDS, USA). The injection rate was 100nl/min. 10min after the end of virus injection, the syringe was retracted slowly to avoid backflow.

The coordinates of virus injection sites were used for virus injection: VTA (AP, –3.20 mm, ML, ±0.25 mm, and DV, –4.4 mm).

Looming test

The looming test was performed as described previously[12]. The looming paradigm consisted of a 40x40x30 cm closed Plexiglas box and with a shelter nest in the corner. An LCD monitor was placed on the ceiling to present upper visual field looming stimulus, which was a black disc on a grey background expanding from a 2° to 20° visual angle, repeated 15 times, lasting 5.5 seconds. Behaviors were recorded using a Sony FDR-AX45 camera. Mice were handled and habituated for 10 min to the looming box the day before the test. During looming tests, mice was allowed freely explore the looming box for 3 minutes, and the looming stimuli were presented for 2 trials with the inter-trial intervals no less than 3 minutes.

The following experimental groups were included in looming tests: young (3-month) and aged (14-month) wild-type mice, OCN$^{-/-}$, GPR37$^{-/-}$, GPR158$^{-/-}$, GPR37 flox/flox, and KCNK13 flox/flox mice.

Looming Behavioral analysis

Behavioral analysis of the looming test was performed as described previously[12,76]. Behavioral data were recorded and analyzed with Adobe Premiere. The following parameters were calculated to define the looming evoked defensive behavior: (i) flight latency: time from the looming presentation to onset the flight to the nest, (ii) return time: time from the onset of looming until returning to the nest, (iii) time in the nest: time spent in the nest following escape. Data obtained from mice with imprecise cannula placement or virus expression were not used for analyses.

Fiber photometry

For the purpose of monitoring neuronal cAMP and calcium dynamics in the VTA, GAD-Cre mice received an intermediate injection of a mixture of AAV9-hsyn-DIO-GFlamp2 and AAV9-hsyn-DIO-NES-SomaFRCaMPi into the VTA region, and OCN-KO mice received an intermediate injection of a mixture of AAV9-mDlx5/6-GFlamp2-WPRE-pA and AAV9-mDlx5/6-NES-SomaFRCaMPi into the VTA region.

Three weeks following viral injection, optical fibers were implanted into the VTA of the same virus injection points. These fibers were then fixed to the skull using skull screws and dental cement to ensure stability. Mice then were allowed a recovery period of no less than 2 weeks prior to the looming testing.

One day before the looming test, mice were acclimated to the optical fiber within the looming stimulus box for at least 15 minutes. To eliminate the background fluorescence of the optical fiber, the fiber was photobleached with intense light for at least one hour. On the test day, each mouse was first given a 3-minute habituation period in the box to reduce stress-induced behavioral artifacts. 2 trials of looming stimuli were then delivered at intervals of 3 minutes. Neural activity during the test was recorded using a fiber photometry system (manufactured by Thinker Tech Bioscience Co., Nanjing, China) operating at a sampling rate of 50 Hz. This neural recording was synchronized with digital video capture to enable simultaneous quantification of behavioral responses. To mitigate fluorescence bleaching, the excitation power was controlled to a range of 20–40 μW at the tip of the optical fiber.

Raw calcium/cAMP fluorescence signals were processed using MATLAB software (MathWorks, Natick, MA, USA). The relative change in fluorescence (ΔF/F) was calculated as follows: $(F - F_0)/(F_0 - V_{offset})$, where F_0 represents the baseline fluorescence signal, which was derived from the average signal over a 2-second time window prior to the onset of each looming stimulus.

For data visualization, ΔF/F values are presented as average plots, with a shaded area surrounding each curve to indicate the standard error of the mean (SEM). For quantitative analysis of neural responses to the looming stimulus, the area under the curve (AUC) of ΔF/F values was calculated over the 5.5-second looming stimulus epoch.

3D behavior collection and analysis

This experiment's setup and data analysis protocols were adapted from prior studies.[9,10] To briefly introduce, a circular open field (50 cm diameter × 50 cm height) with transparent acrylic walls and a white plastic base was placed on a movable 90×90×75 cm stainless-steel framework. Four Intel RealSense D435 cameras were mounted at orthogonal angles on the framework's pillars for multi-perspective video capture. A thick, dull-polished black rubber mat was laid between the open field and framework to minimize light reflection. A 56-inch TV, horizontally mounted upside-down on the framework top, provided uniform white background lighting.

Mice were acclimated for 15 min, then allowed 15 min of free movement in the open field. Their spontaneous behaviors were recorded via the multi-view cameras. Images were captured simultaneously at 30 frames per second (fps) using a PCI-E USB-3.0 data acquisition card and the *pyrealsense2* Python package. All devices were connected to a high-performance computer (i7-9700K, 16G RAM, 1TB SSD + 12TB HDD) for data acquisition. Python and OpenCV programs stored videos at 30 fps with 640×480 pixel frames. The apparatus was cleaned with 75% ethanol after each mouse to eliminate residual olfactory/behavioral cues.

Mice spontaneous behaviors were analyzed by BehaviorAtlas Analyzer 1.0 (Shenzhen Bayone BioTech Co., Ltd. Shenzhen, China). Thirty-nine kinematic parameters of the spontaneous behaviors were assessed via machine learning, including: horizontal velocity and 3D movement energy of 16 body points; body center speed, length (nose-to-tail root), height (back-to-floor), and angle (back-neck/back-tail root); freezing index (time ratio with speed <15 mm/s for >2 s); flight index (time ratio with speed >400 mm/s for >0.1 s); and center-time ratio.[77]

Movement fractions (time proportion in each spontaneous behavior cluster) and kinematic features were analyzed automatically via a 3D behavior decomposition framework. Behavioral clusters were manually annotated.[77,78]

Serum OCN detection following acute stimuli

To determine whether acute stimuli induce an increase in blood osteocalcin (OCN) levels, a single group of mice was subjected to three experimental conditions: (1) no stimulus (control condition); (2) five repetitions of a 5.5-second looming stimulus, administered once per minute; and (3) five repetitions of a 1-second electrical stimulus (1 mA), administered once per minute.

Following each experimental condition, mice were anesthetized via i.p. injection of pentobarbital at a dose of 80 mg/kg. Approximately 150 μL of blood was collected from each mouse using the tail vein sampling method. A minimum interval of one week was maintained between consecutive experimental conditions to ensure that the mice were fully recovered. Collected blood samples were centrifuged at 3,000 rpm at 4°C for 20 minutes. The supernatant (serum/plasma) was then harvested and reserved for subsequent OCN concentration determination.

Serum Osteocalcin Measurement

Age-dependent baseline OCN levels

Blood samples were collected from anesthetized wild-type mice at 3, 7, and 14 months of age via the orbital venous plexus to assess developmental changes in osteocalcin levels.

Acute stress-induced OCN measurement

To evaluate rapid changes in circulating OCN following acute stressors, a separate cohort of mice underwent serial tail vein blood collection at specified time points after stimulation. Mice were exposed to one of three conditions: (1) no stimulus (baseline control); (2) five 5.5-s looming stimuli delivered at 1-min intervals; or (3) five 1-s foot shocks (1 mA) delivered at 1-min intervals. Different experimental conditions were separated by ≥1 week recovery period.

Sample processing and analysis

All blood samples were centrifuged at 3000 × g for 20 min at 4°C to isolate serum. Bioactivated osteocalcin levels were quantified using the Mouse Glu-Osteocalcin High Sensitive EIA Kit (Takara, #MK-129) according to manufacturer instructions. Absorbance was measured at 450 nm using a microplate reader, with all samples analyzed in duplicate.

In vivo Treatments

To assess the effect of osteocalcin on innate defensive behavior, 7- and 14-month-old wild-type mice were intraperitoneally injected with either vehicle or osteocalcin (50 ng/g, Super Peptides Co.,Ltd, China) daily for 10 days prior to looming tests[3].

Cannula implants and pharmacology

Both OCN-/- and GPR37-/- mice were used for pharmacological experiments. Cannulas were implanted bilaterally 0.2 mm above the VTA using the following stereotaxic coordinates (relative to Bregma): AP, –3.20 mm; ML, ±0.25 mm; DV, –4.2 mm. After surgery, mice were allowed to recover for at least 2 weeks. Following post-operative handling and behavioral habituation, osteocalcin or saline was infused into the cannulas 0.5 hours prior to the looming test to evaluate its effect on visual threat-induced defensive behavior in VTA-specific rescue paradigms.

Electrophysiological recordings

Acute brain slices of VTA were prepared as described in previous studies[1]. Male GAD-Cre, GPR37-/- and GPR158-/- mice with GABAergic neurons labelled with GFP were anaesthetized with isoflurane and perfused immediately with ice-cold aCSF (artificial cerebrospinal fluid), which contained (in mM): 125 NaCl,2.5 KCl,1.3 NaH_2PO_4,1.3 Na-ascorbate, 0.6 Na-pyruvate,2 $CaCl_2$,2 $MgSO_4$, 10 glucose, 25 $NaHCO_3$ (oxygenated with 95% O_2 and 5% CO_2, pH 7.35, 295–305 mOsm). Acute brain slices (270 μm) containing the VTA were cut using a cutting solution containing (in mM): 110 choline chloride, 2.5 KCl, 1.3 NaH_2PO_4, 1.3 Na-ascorbate, 0.6 Na-pyruvate, 0.5 $CaCl_2$, 7 $MgCl_2$, 25 glucose, 25 $NaHCO_3$, 3 myo-inositol and saturated by 95% O_2 and 5% CO_2. Slices were then maintained in the holding chamber filled with aCSF for 1 hour at 34°C.

For electrophysiological whole-cell recordings, slices were transferred into a recording chamber fitted with a constant flow rate of aCSF (2.5 ml/min, 34°C) equilibrated with 95% O_2 and 5% CO_2. Glass microelectrodes (4–6 MΩ) were filled with internal solution containing (in mM): 130 K-gluconate, 10 KCl, 10 HEPES, 1 EGTA, 0.3 Na-GTP, 2 Mg-ATP, 2 MgCl2 (pH 7.2, 285 mOsm). Whole-cell electrophysiological recordings were obtained only from GFP-positive VTA neurons.

Electrophysiological signals were recorded using a Multiclamp 700B amplifier (Molecular Devices). All recordings were filtered at 3 kHz (Bessel filter) and sampled at a rate of 50 kHz. Signal acquisition was performed using pClamp 10.2 software (Molecular Devices). The series resistance during recordings ranged from 10 to 20 MΩ. To ensure data quality, any recording was excluded from subsequent analysis if the series resistance increased by more than 20% over the course of the recording session.

For the purpose of spontaneous action potential recordings, VTA-positive neurons were patched without applied holding current (I = 0 pA). 5 min continuous recordings were obtained before and after application of pharmacological agents.

For the purpose of sEPSC and sIPSC recordings, the internal solution contained the following (in mM): 135 CsCl, 0.5 $CaCl_2$, 10 HEPES, 0.5 EGTA, 0.3 Na-GTP, 2 Mg-ATP, 5 QX-314. VTA-GFP positive neurons were held at -70 mV for sEPSC recording with 10 μM bicuculline added to the external solution, and held at 0 mV for sIPSC recordings with 50 μM DL-AP5 and 10 μM CNQX in the external solution. 5 min continuous recordings were obtained before and after OCN application.

To record step-induced action potentials, 50 μM DL-AP5, 10 μM CNQX and 10 μM bicuculline were included in the external solution to block synaptic transmission. VTA-GFP positive neurons were held at -70 mV and a series of 1 s pulses from 0 pA to +200 pA with an increment of 25 pA was applied to record the changes in resting membrane potential and numbers of action potential (elicited by positive currents) before and after pharmacological tool application.

In order to record gross K^+ current, the external solution was supplemented with 1 μM tetrodotoxin (TTX), 200 μM $CdCl_2$ and 100 μM NPPB to block Na^+ channels, Ca^{2+} channel and Cl^- channels, respectively. Series resistance was between 20 and 40 MΩ and was ~70% compensated. A series of 4 s voltage pulses from -90 mV to 110 mV with an increment of 10 mV was applied in the absence and presence of OCN.

For KCNK13 current isolation, 1 μM CVN293 (a specific KCNK13 blocker) was applied. KCNK13 current was calculated by subtracting currents recorded after 10 min CVN293 application from those recorded before. For GIRK1 current isolation, 0.2 μM tertiapin-Q (TPN-Q, a specific GIRK1 blocker) was applied. GIRK1 current was determined by subtracting post-TPN-Q (10 min) currents from pre-TPN-Q currents.

Tissue dissection from adult VTA

Mice were anesthetized with pentobarbital (i.p., 80 mg/kg), and brains were rapidly removed and put in the ice cold DEPC-PBS. Brains were cut into 1 mm thick coronal sections on mouse brain matrix (RWD, China). The sections containing the VTA (ranging from -2.92 to -3.88 anterior posterior to Bregma) were micro-dissected from neighboring brain regions (n=20 mice). Every dissected VTA tissue were collected in ice cold centrifuge tubes and then transferred to vacuum cup filled with liquid nitrogen. Total dissected VTA were stored at -80°C for single nucleus RNA-seq processing andwestern blotting.

Single cell nucleus RNA-seq

Dissected VTA tissues were collected and dissociated using an adult brain dissociation kit from Miltenyi Biotec (Bergisch Gladbach, Germany). Subsequent procedures were performed by AccuraMed (Shanghai, China). Briefly, single-cell gel beads in emulsions (GEMs) and Barcoding were firstly generated. Master Mix were prepared, and Single-Cell suspension ran in the Chromium Controller (10X Genomics). GEMs transferred and Post GEM-RT cleanup& cDNA amplification conducted following standard protocols. Gene expression library was constructed, and every library was sequenced on a HiSeq X Ten platform (Illumina)

Bioinformatic analysis

Initial processing of snRNA-seq data

Using the official analysis software CellRanger (version 3.1.0) provided by 10x Genomics, the raw data was filtered, mapped, quantified, and identified and recovered cells, and finally the gene expression matrix of each cell was obtained. The specific implementation method is as follows: Extract 10x Barcode and UMI sequence at the R1 end, as well as the insert sequence at the R2 end for gene alignment. Use STAR aligner (Spliced Transcripts Alignment to a Reference) to map reads (R2 insert of 91bp extracted in the previous step) to the reference genome (GRCm38), and use genomic GTF annotation files to correct to distinguish exon regions, intron regions, and intergenic regions. The Barcode sequence information obtained by sequencing is compared with the known Barcode sequence in the database, and the barcode sequence (measured sequence) that exactly matches the known Barcode in the database is the real sequence. The sequenced UMI sequence can not be used directly for subsequent analysis, and unqualified reads need to be filtered and corrected. Count all valid barcodes to obtain an unfiltered blast gene expression matrix, only read that contains valid barcodes and UMIs and are reliably aligned can be counted. A distinction between barcodes containing cells and background barcodes is required to extract formal single-cell data for downstream analysis.[79]

Data QC and filtering

We generated scatter plots of the number of transcript molecules per cell (n_counts), the percentage of transcripts from mitochondrially encoded genes (percent_mito), and the number of expressed genes (n_genes) to identify outlier cells. Cells meeting the following criteria were retained: 100 < n_genes < 8000, percent_mito < 1%, and n_counts < 40,000. Only genes detected in more than three cells were kept for further analysis. We used scanpy.external.pp.scrublet() to identify doublets, setting the doublet score threshold to 0.15 and retaining cells with a score below this threshold, labeled as 'False'. Cells were normalized for library size differences, with transcript counts in each cell rescaled to sum to 10,000, followed by log-transformation.

Merging Two Bio-replicates and Cell Class Annotation

We used scanpy. AnnData.concatenate() to merge two bio-replicates, identified highly variable genes (HVGs), and computed a reduced dimensional representation of the data using principal component analysis (PCA). Harmony was then applied to adjust the principal components, storing the result as 'X_harmony'. This representation was used to compute a nearest-neighbor graph of the cells, which was subsequently clustered using the Leiden algorithm and embedded in 2D via the Uniform Manifold Approximation and Projection (UMAP) algorithm.

After that, neurons and non-neurons were classified based on canonical marker genes, with the Leiden algorithm resolution parameter set to 0.5. Neurons were then re-ustered with the resolution parameter increased to 0.8. All neurons were annotated into four classes: Glut, GABA, GABA-Glut, and Dopa using canonical marker genes. Finally, based on the number of principal components from PCA that explained the most variance, the GABA-Glut cells were clustered into three clusters with a resolution set to 0.1. The scanpy.tl.rank_genes_groups() function and the Wilcoxon rank-sum test with tie correction in the Scanpy package were then used to identify marker genes.

Calculating Gene Expression Correlation

The GABA-Glut cells were assigned into specific bin according to the UMAP1 and UMAP2 axes with a step size of 1, and the average expression of Gpr37, Gpr158, and all K channel genes was calculated for each bin. The correlation coefficients and p-values for the expression of all K channel genes with Gpr37 and Gpr158 were computed using the spearmanr function in scipy.stats, with a p-value threshold set at 0.01. The slope and intercept of linear regression fitting were calculated using numpy.polyfit.

In situ sequencing

The specific probes for target RNA were designed by spatial FISH Ltd. Samples were fixed by 4% paraformaldehyde, then covered with reaction chamber to perform the following reactions. After dehydration and denaturation of samples with methanol, the hybridization buffer with specific targeting probes was added to the chamber for incubation at 37°C overnight. Then samples were washed three times with PBST, followed by ligation of target probes in ligation mix at 25°C for 3 h. Next, samples were washed three times with PBST and subjected to rolling circle amplification by Phi29 DNA polymerase at 30 °C for overnight. Subsequently, the fluorescent detection probes in hybridization buffer was applied to samples. Finally, samples were dehydrated with an ethanol series and mounted with mounting medium. After capturing images by Leica THUNDER Imaging Systems, signal dots were decoded to interpret RNA spatial position information.[80]

Image Alignment

We used ImageJ to process multi-channel z-stack images (containing z, y, x dimensions). The images were maximum projected along the z-axis to generate 2D multi-channel images, and contrast parameters were adjusted to enhance fluorescence signals. The processed results were saved in.tif format (e.g., 'demo_A_a-gene_b-gene_c-gene.tif'). Next, we used the BigWarp plugin for image alignment. Corresponding points were selected for alignment, and the results were exported and named 'demo_B_moving_d-gene_e-gene_f-gene.tif'.

Fluorescence Signal Detection and Statistics

The bigwarp-calibrated tif images were input into the U-FISH system for standardized image output and automated analysis, with results saved accordingly. For dense or weak fluorescence signals, the RS-FISH plugin in ImageJ was used for manual single-channel image calling, parameter adjustment, and result saving. In U- FISH result files, axis-0 represents the channel, and axis-1 and

axis-2 represent the y and x coordinates, respectively; RS-FISH results include x, y, t, c, and intensity information. Gene information was assigned to the corresponding channels by adding a 'gene' column at the end of the file, and the results were merged into 'all_gene_location.csv'.

Cell Segmentation

In ImageFlow, after loading the required packages, the DAPI tif image was read using AICS:ReadImage, and cell nuclei were segmented using cellpose. The segmentation results were visualized using Viewer:Standalone Napari and saved as 'mask.tif'. Then, the gene coordinate file was read using pandas:read_csv, and genes were assigned to cells using innereye:gene_to_cell, with the statistical results saved.

Visualization Analysis

ClusterMap algorithm was used for visualization analysis in the Python environment. The coordinates of all successfully decoded gene points and the DAPI image were input. The ''ClusterMap'' function was used to segment points into individual cells, with parameters set to a radius of 15 and a window size of 60. Cells meeting quality standards were normalized and scaled, and batch effects were corrected using the combat function. PCA was performed using the ''arpack svd_solver'', focusing on the top five principal components (PC1-PC5). Cells were clustered using the Louvain algorithm (resolution 0.6), and UMAP was generated for visualization. The ''rank_genes_groups'' function was used to identify differentially expressed genes (DEGs) specific to each cluster, using the Wilcoxon test method.

Cell Type Annotation

Gene spot assignment was performed using KDTree in the Python environment, following approaches described in the articles ''Spatial multi-omics at subcellular resolution via high-throughput in situ pairwise sequencing''[81]. After input all decoded gene spot coordinates and segmented DAPI images, the KDTree function was used to calculate the Euclidean distance and identified the nearest cell for each gene spot. A gene spot was assigned to a cell if its distance to that cell was less than a threshold (30 pixels). Unassigned signal spots were iteratively assigned using successfully assigned signal spots as target points (with a query distance of 10 pixels and 5 iterations). Finally, signal spots that could not be assigned to any cell were discarded.Cells were annotated based on cell-type marker gene sets. When multiple cell-type markers were detected within a cell, annotation was determined by the Euclidean distance of the gene from the cell centroid: the closer a gene was to the nucleus (DAPI center), the lower the probability of erroneous assignment. Specifically, cells are defined by key marker genes: *TH* for TH cells, *Mog* for oligodendrocytes (Oligo), *GAD2* for GAD2 cells, and *Slc17a6* for VGlut2 cells. Additionally, distinct GABA-Glut subpopulations were defined by the co-expression of *GAD2* and *Slc17a6* with a third marker: *Pdzd2* for GABA-Glut-0, *B230217J21Rik* for GABA-Glut-1, and *QK* for GABA-Glut-2.

Western Blot

Ventral tegmental area (VTA) tissues were rapidly micro-dissected from the brains of Gpr37-/- and KCNK13 flox/flox mice and immediately snap-frozen in liquid nitrogen. For Western blot analysis, tissues were homogenized in ice-cold RIPA lysis buffer (Beyotime, P0013B) supplemented with PMSF (Beyotime, ST505). Lysates were centrifuged at 14,000 × g for 15 min at 4°C, and supernatants were collected. Protein concentration was determined using a BCA Protein Assay Kit (Beyotime, P0010) on an INFINITE E PLEX microplate reader (Tecan, asset S20230629). Equal amounts of protein (10 μg per lane) were separated on 10% SDS-PAGE gels (BioTeke, PG112) and transferred to PVDF membranes (Beyotime, FFP32). Membranes were blocked and then incubated overnight at 4°C with the following primary antibodies: mouse anti-GPR37 (1:1000), rabbit anti-KCNK13 (1:2000) and mouse anti-GAPDH (1:10000; Beyotime, AF2819). After washing with TBST (Epizyme, PS103P), membranes were incubated with HRP-conjugated secondary antibodies (HRP Goat Anti-Rabbit or Anti-Mouse IgG; Abclonal, AS003). Protein bands were visualized using enhanced chemiluminescence and imaged on an Amersham Image Quant 800 system (Cytiva, asset S20230622).

Quantitative Real-Time PCR

Total RNA was extracted from VTA tissues using the SteadyPure Rapid RNA Extraction Kit (AG21023, Accurate Biotechnology). cDNA was synthesized from 1 μg of total RNA using the Evo M-MLV Reverse Transcription Premix (AG11706, Accurate Biotechnology). Quantitative PCR was performed using the SYBR Green Pro Taq HS Premix qPCR Kit (AG11701, Accurate Biotechnology) on a QuantStudio 7 Flex Real-Time PCR System (Applied Biosystems, asset S20230262). Reactions were carried out in 0.2 mL transparent qPCR plates (AG12118, Accurate Biotechnology) under the following conditions: 95°C for 30 s, followed by 40 cycles of 95°C for 5 s and 60°C for 30 s. The primer sequences were: Gpr37 forward, 5′-AACCTGGCTTTCTGGGACTT-3′ and reverse, 5′-ATCTG GACGTTGGTGGCAG-3′; Gapdh forward, 5′-TGTGTCCGTCGTGGATCTGA-3′ and reverse, 5′-TTGCTGTTGAAGTCGCAGGAG-3′. The relative mRNA expression levels of Gpr37 were calculated using the $2-\Delta\Delta Ct$ method, with Gapdh as the endogenous control and the LV-GFP group designated as the calibrator for all comparative analyses. All reactions were performed in technical triplicates.

Histology and immunostaining

Mice were overdosed with pentobarbital and perfused with 0.9% saline followed by 4% paraformaldehyde (PFA) in PBS. Brains were dissected and postfixed in 4% PFA at 4 °C for 24 h and transferred to 30% sucrose for 2 d. We cut 40-μm coronal slices of the entire rostrocaudal extent of the brain via a cryostat at –15 °C and stored in 24- well plates containing cryoprotectant at 4 °C.

To visualize virus expression, cannula placements, floating sections blocked with 10% normal goat serum in PBS-T (0.3% Triton-X 100) and DAPI (1:50000, Cat#62248, Thermofisher). If needed, brains slices were kept at 4 °C overnight with the following antibodies mouse anti-TH, mouse anti-GAD67, rabbit anti-GPR37 (Cat#64407, Cell Signaling Technology). The secondary antibodies Alexa fluor 488 or Alexa fluor 594 or Alexa fluor 647 were used. Sections were mounted and covered slipped with Fluoromount aqueous mounting medium (Sigma-Aldrich, USA). Sections were then photographed by Olympus VS120 virtual microscopy slide scanning

Please cite this article in press as: Liu et al., A bone-derived hormone permits rapid visual escape via GPR37 receptor in a subpopulation of VTA GABAergic neurons, Neuron (2025), https://doi.org/10.1016/j.neuron.2025.12.048

system or Zeiss LSM 880 confocal microscope. Images were analyzed with and ImageJ, Image Pro- plus, and Photoshop software.

Neuronal culture and Biotinylated Osteocalcin treatment

Bilateral ventral tegmental area (VTA) was dissected from 2-month-old mice. VTA from 5-6 mice were collected and dissociated with 0.25% Trypsin/EDTA for 30 min at 37°C. Cells were pelleted and resuspended in DMEM supplemented with 10% fetal bovine serum, penicillin/streptomycin and then plated on poly-d-lysine-coated glass coverslips in a 24-well plate at a density of 7 × 104 cells/well. Cultures were maintained for 2 hours at 37°C with 5% carbon dioxide atmosphere. Cells were then treated with biotinylated Osteocalcin (Biotin Protein Labeling Kit, Cat# 11418165001, Roche, USA) with different concentration for 30 min at 37°C.

For immunostaining, cells were fixed for 20 min in 4% paraformaldehyde. After fixation, cells were incubated in a blocking solution (3% normal goat serum in tris buffer saline solution with 0.1% Triton X-100) for 1 hour at room temperature.

Primary antibodies mouse anti-TH antibody (MAB318, Millipore), mouse anti- GAD67 antibody (MAB5406, Millipore) were used to identify the cell type. They were co-stained with rabbit anti-GPR37 (Cat#64407, Cell Signaling Technology) and Alexa 488 conjugated streptavidin overnight at 4°C. Afterward, cells were incubated with fluorochrome-conjugated secondary antibodies for 2 hours at room temperature and mounted in mounting media. Z-stacked images were obtained with a Zeiss LSM 880 Airyscan confocal microscope (Zeiss, Germany).

Cell counting

For counting cell in the VTA, 40 μm coronal sections from bregma -2.9 to -3.8 mm for each mouse were collected for immunohistochemistry. The brain sections were mounted and imaging using a Zeiss LSM 880 Airyscan confocal microscope and Olympus VS120 virtual microscopy slide scanning system. Then the immunostaining was analyzed and counted with image J, image Pro-plus and Photoshop software.

QUANTIFICATION AND STATISTICAL ANALYSIS

All looming behavioral videos were analyzed frame by frame manually using Adobe Premiere. All statistics were performed in Graph Pad Prism (GraphPad Software, Inc.). Paired student test, unpaired student test and one-way ANOVA were used where appropriate. Mixed-effect modeling (under two-way ANOVA category in GraphPad Prism) was used to compare changes in neuronal excitability and ion channel current induced by pharmacological tool application. Multiple comparisons with Sidak test for post-hoc corrections were further performed when Interaction (Row Factor * Column Factor) was significant in Two-way ANOVA test. It was stated as two-way ANOVA with Sidak test for post-hoc corrections in the text when used. In all statistical measures a P value <0.05 was considered statistically significant. Post hoc significance values were set as *P< 0.05, **P< 0.01, ***P< 0.001 and ****P< 0.0001; all statistical tests used are indicated in the Figure legend.